JOURNAL OF CLINICAL NEUROPHYSIOLOGY

Official publication of the American Clinical Neurophysiology Society

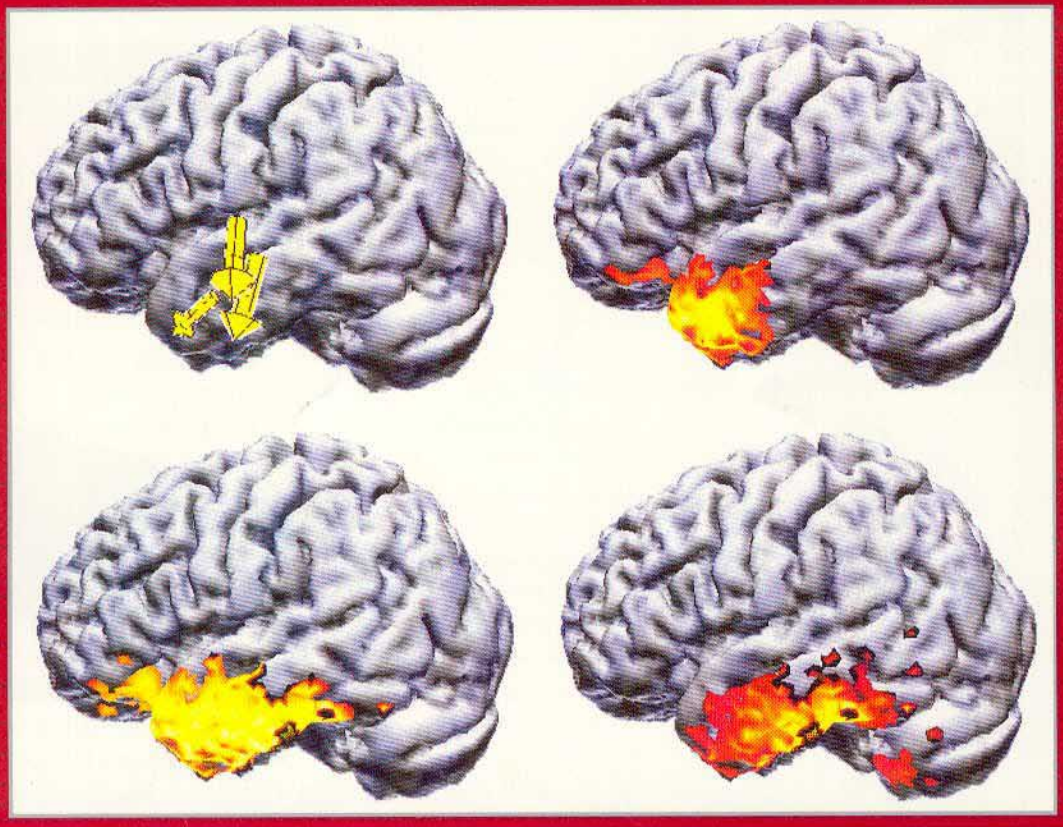

EEG Source Modeling

Volume 16 / Number 3 / 1999

LIPPINCOTT WILLIAMS & WILKINS

Journal of Clinical Neurophysiology
16(3):267–295, Lippincott Williams & Wilkins, Inc., Philadelphia

Linear and Nonlinear Current Density Reconstructions

Manfred Fuchs, Michael Wagner, Thomas Köhler, and Hans-Aloys Wischmann

Philips Research Laboratories Hamburg, Germany

Summary: Minimum norm algorithms for EEG source reconstruction are studied in view of their spatial resolution, regularization, and lead-field normalization properties, and their computational efforts. Two classes of minimum norm solutions are examined: linear least squares methods and nonlinear L_1-norm approaches. Two special cases of linear algorithms, the well known Minimum Norm Least Squares and an implementation with Laplacian smoothness constraints, are compared to two nonlinear algorithms comprising sparse and standard L_1-norm methods. In a signal-to-noise-ratio framework, two of the methods allow automatic determination of the optimum regularization parameter. Compensation methods for the different depth dependencies of all approaches by lead-field normalization are discussed. Simulations with tangentially and radially oriented test dipoles at two different noise levels are performed to reveal and compare the properties of all approaches. Finally, cortically constrained versions of the algorithms are applied to two epileptic spike data sets and compared to results of single equivalent dipole fits and spatiotemporal source models. **Key Words:** EEG—Current density reconstructions—Regularization—Minimum norm—LORETA.

Equivalent dipole models are commonly used for EEG- and MEG-source reconstruction. Different approaches can be found with differing degrees of freedom of the sources. Moving dipoles, representing a single time slice only, are the most simple source model. Spatiotemporal methods with rotating or fixed dipoles are the next step representing additional physiological a priori constraints (Scherg and von Cramon, 1985; Mosher et al., 1992). Rotating dipoles have fixed positions over a selected latency range, but their components are free to change independently, whereas fixed dipoles exhibit fixed orientations over the selected time range as well. For all these models of brain activity the nonlinear source position parameters can be fitted by a multidimensional minimization procedure (e.g., Nelder and Mead, 1965), whereas the linear source component parameters are calculated via an over-determined system of equations. With d dipoles, c dipole components per dipole ($c=1$ for known dipole orientations (gray matter layer normals), $c=2$ for MEG with spherical volume conductor geometry, $c=3$ otherwise), and t measured samples, a moving dipoles model has $3*d*t$ nonlinear parameters and $c*d*t$ linear parameters. A rotating dipoles approach comprises $3*d$ nonlinear and $c*d*t$ linear parameters. Finally, a fixed dipoles model exhibits $3*d + (c-1)*d$ nonlinear and $d*t$ linear parameters. For more than one fixed dipole, the best fit orientation of each dipole has to be fitted as additional nonlinear parameter ($(c-1)*d$).

All equivalent dipole algorithms need an a priori knowledge of the number and class of sources involved in the brain activity to be reconstructed. Thus often principal component analyses (PCA) or singular value decompositions (SVD) are used before the dipole fit to obtain a first evaluation of the number (and strengths) of field patterns that are contained in the measured data, without applying a specific source model (Mosher et al., 1992). The number of field patterns with strengths above

Address correspondence and reprint requests to Manfred Fuchs, Philips Research Laboratories Hamburg, Röntgenstr. 24, 22335 Hamburg, Germany

the measurement noise represents the minimum number of noncoherent fixed dipoles that are used to explain the data.

Anatomical a priori knowledge of the source positions (and orientations) cannot be involved in these equivalent dipole methods directly. However, by evaluating the least squares error function to be minimized at given positions only, e.g., the gray matter layer segmented from magnetic resonance images (MRI), the areas of interest can be scanned. The nonlinear parameters no longer need to be fitted then, but only the overall best fit positions have to be found.

An increasing interest in current density reconstruction algorithms has occurred during the last several years. From two-dimensional (2D)-approaches and Fourier methods (Dallas, 1985; Kullmann and Dallas, 1987; Gorodnitzky et al., 1992), simplified cortical folds (Wang et al., 1992) and three-dimensional (3D) distributions were tackled (Jeffs et al., 1987; Smith et al., 1990; Hämäläinen and Ilmoniemi, 1994; Pascual-Marqui et al., 1995; Sekihara and Scholz, 1996; Phillips et al., 1997; Grave de Peralta Menendez et al., 1997, 1998). All these methods have in common that elementary dipoles are distributed on given positions, e.g., on regular grids inside the head or in cortically constrained implementations on the gray matter layer (Dale and Sereno, 1993; Fuchs et al., 1994*a*, 1995). The calculation of the strengths and orientations of these dipoles generally leads to a highly underdetermined system of equations (number of unknown dipole components $c*d$ is much larger than the number of sensors s). It can be solved by additional, appropriate constraints only. By applying these (e.g., minimum norm) constraints, mathematically unique solutions can be achieved. The additional, constraining model term has to be weighted against the data term, which is done by a so called regularization parameter. In a signal-to-noise-ratio (SNR) framework (Morozov, 1968; Pflieger et al., 1996; Fuchs et al., 1998*b*), the critical choice of the regularization parameter can be automated with some methods, so that no overfitting or underfitting of the data occurs. Otherwise, this parameter has to be adjusted manually to achieve an adequate representation of the measured data.

Current density methods are commonly applied to single time-point evaluations, but do not need the number of sources as additional input. Also no assumptions about the shape or size of an activated area are made, whereas single equivalent dipoles are based on the implicit assumption that patches of activated gray matter are well represented by their centers of gravity and their mean surface normals. Another hope is that one can estimate the extents of the active brain areas with current density reconstructions as well. Due to the underdetermined character of the problem and the blurring properties of the minimum norm least squares constraint, this class of source reconstruction algorithms yields smooth current distributions in contrast to the rather overfocussing equivalent dipole methods.

The number of parameters (the dipole components) to be calculated with the least squares approaches is $c*d(*t)$. It can be accomplished for each time slice by solving a linear system of equations by matrix inversion or singular value decomposition. If another norm is used instead of the L_2-norm of the least squares methods, e.g., the L_1-norm, a nonlinear system of equations with the same number of unknowns has to be solved. Therefore, the latter methods need much more computational efforts. However, the L_1-norm approaches promise much more focal solutions and a more robust behavior against outliers in the measured data.

The spatial resolution power of the different current density reconstruction methods is studied with noisy data, which is a more realistic approach compared to the more theoretical, noisefree resolution operator concept (Backus and Gilbert, 1967; Grave de Peralta Menendez et al., 1997, 1998).

METHODS

The first part of this section will deal with linear current density methods, where closed formulations for the minimum norm solutions can be achieved. The nonlinear L_1-norm methods will be discussed in the second part. The third part explains the setup and methods used for the simulations and their evaluations. Finally, the fourth part describes the approaches applied to the two sets of epileptic spike data.

Generalized Minimum Norm Formulation

In a generalized formulation the data term D, that accounts for deviations between measured data $\underline{M}$ (column vector of the s sensors) and calculated sensor signals $\underline{S} = \underline{\underline{L}}*\underline{j}$ (with the lead-field matrix $\underline{\underline{L}}$ $(s*(c*d)$, comprising dipole positions and volume conductor properties, and the column vector $\underline{j}$ of the $c*d$ current components), can be written as:

$$D = \|\underline{\underline{W}}*(\underline{M} - \underline{S})\|_m^p \qquad (1)$$

The matrix $\underline{\underline{W}}$ is an s^2-weighting matrix for the s sensors, m denotes the norm used for the weighted differences and p is the power applied to the data term.

The minimum norm model term T contains the

weighting matrix $\underline{\underline{C}}$ $((c*d)^2)$ for the current components, n describes the norm used, and q is the power applied to the model term:

$$T = \|\underline{\underline{C}}*\underline{j}\|_n^q \quad (2)$$

Both terms have to be minimized simultaneously and are weighted by the positive regularization parameter λ:

$$minimize\ \Delta = D + \lambda*T$$

$$= \|\underline{\underline{W}}*(\underline{M} - \underline{S})\|_m^p + \lambda*\|\underline{\underline{C}}*\underline{j}\|_n^q \quad (3)$$

Minimum Norm Least Squares

The commonly used minimum norm least squares case ($m=n=p=q=2$) leads to Frobenius norms for both data and model terms. The Frobenius norm of a $u*v$ matrix $\underline{\underline{A}}$ is given by:

$$\|\underline{\underline{A}}\|_2^2 = \sum_{i=1}^{u}\sum_{k=1}^{v} a_{ik}^2 \quad (4)$$

With nonsingular weighting matrices $\underline{\underline{W}}$ and $\underline{\underline{C}}$, the solution of Eq. 3 for the best fit current components, in this special case, is given by (Lawson and Hanson, 1974; Tarantola, 1994):

$$minimize\ \Delta = \|\underline{\underline{W}}*(\underline{M} - \underline{\underline{L}}*\underline{j})\|_2^2 + \lambda*\|\underline{\underline{C}}*\underline{j}\|_2^2 \quad (5)$$

$$j = (\underline{\underline{C}}^T*\underline{\underline{C}})^{-1}*\underline{\underline{L}}^T*\underline{\underline{W}}^T*\underline{\underline{X}}^{-1}*\underline{\underline{W}}*\underline{M} \quad (6)$$

$$with\quad \underline{\underline{X}} = \underline{\underline{W}}*\underline{\underline{L}}*(\underline{\underline{C}}^T*\underline{\underline{C}})^{-1}*\underline{\underline{L}}^T*\underline{\underline{W}}^T + \lambda*\underline{\underline{1}} \quad (7)$$

With no detector and no current component weighting ($\underline{\underline{W}}=\underline{\underline{1}}$ and $\underline{\underline{C}}=\underline{\underline{1}}$) the standard solution for the minimum nom least squares case is easily obtained:

$$minimize\ \Delta = \|\underline{M} - \underline{\underline{L}}*\underline{j}\|_2^2 + \lambda*\|\underline{j}\|_2^2 \quad (8)$$

$$\underline{j} = \underline{\underline{L}}^T*(\underline{\underline{L}}*\underline{\underline{L}}^T + \lambda*\underline{\underline{1}})^{-1}*\underline{M} \quad (9)$$

This standard solution is known to lead to superficial source distributions because small currents close to the detectors can produce fields of similar strengths as larger currents at greater depths, which will thus be suppressed by the unweighted minimum norm term in Eq. 8. To compensate for the undesired depth dependency of this approach, the currents can be weighted to account for the lower gains of deeper dipole components (lead-field normalization) (Gorodnitzky et al., 1992; Fuchs et al., 1994*b*).

$$minimize\ \Delta = \|\underline{M} - \underline{\underline{L}}*\underline{j}\|_2^2 + \lambda*\|\underline{\underline{C}}*\underline{j}\|_2^2 \quad (10)$$

$$\underline{j} = (\underline{\underline{C}}^T*\underline{\underline{C}})^{-1}*\underline{\underline{L}}^T*(\underline{\underline{L}}*(\underline{\underline{C}}^T*\underline{\underline{C}})^{-1}*\underline{\underline{L}}^T + \lambda*\underline{\underline{1}})^{-1}*\underline{M} \quad (11)$$

With a location- or component-wise depth weighting, the large $((c*d)^2)$ matrix $\underline{\underline{C}}$ is diagonal and therefore $(\underline{\underline{C}}^T*\underline{\underline{C}})^{-1}$ can be calculated very easily. The other matrix inversion $(\underline{\underline{L}}*(\underline{\underline{C}}^T*\underline{\underline{C}})^{-1}*\underline{\underline{L}}^T + \lambda*\underline{\underline{1}})^{-1}$ is applied for a much smaller (s^2) matrix only and is thus very fast, since the number of sensors s is usually in the order of 100.

Laplacian Smoothness

The same solution as in the case with weighted current components (Eqs. 10 and 11) is achieved for a different method, which uses the second order spatial derivatives (Laplacians) of the current components to achieve a smooth current distribution (Messinger-Rapport and Rudy, 1988; Pascual-Marqui et al., 1995). In this special case of the formulation described above, the weighting matrix $\underline{\underline{C}}$ is set up to use these derivatives by a discrete formulation of the Laplacian. With source positions on regular 3D-grids a 3^3 kernel is used for this purpose. The boundaries of the volume conductor limit the source space, so that special care has to be taken there. The nonzero elements of the matrix $\underline{\underline{C}}$ are ("LORETA", Pascual-Marqui et al., 1995):

$$C_{ii} = -1 \quad and \quad C_{ij} = (6 + N_i)/(12N_i) \quad (12)$$

for all locations i, with j denoting the N_i (maximal 6) direct neighbors of location i.

In a gray matter constrained implementation, a volume with high gray matter probability is derived from a statistical brain data set (Collins et al., 1995) and serves as the boundary of the regular 3D grid. For a true cortically constrained implementation that allows sources to be oriented perpendicular to the cortical sheet and measures smoothness along the cortex, a 2D surface Laplacian has to be computed. Here, the spatial distances on the folded gray matter layer are used and neighborhood relations are taken from a triangle mesh covering the cortex (Wagner et al., 1996). Now the nonzero elements of $\underline{\underline{C}}$ are (Huiskamp, 1991) $C_{ii} = -1$ and $C_{ij} = 1/N_i$, or in a distance weighted formulation:

$$C_{ii} = \frac{-1}{\sum_{j=1}^{N_i} d_{ij}} \sum_{j=1}^{N_i} \frac{1}{d_{ij}} \quad and \quad C_{ij} = \frac{1}{d_{ij}\sum_{j=1}^{N_i} d_{ij}} \quad (13)$$

with N_i neighbor-nodes, and d_{ij} the distance between locations i and j.

Since with the Laplacian method the minimum norm applies to a more indirect measure (second order derivatives of the current strengths) as compared to the standard formulation (strengths are used directly in the

model term), a smaller effect of the here also applicable lead-field normalization can be expected.

The computational effort for the Laplacian methods is much larger than for standard weighted minimum norm approaches, because the weighting matrix $\underline{\underline{C}}$ is not diagonal but sparse, and $(\underline{\underline{C}}^T*\underline{\underline{C}})^{-1}$ has to be calculated explicitly. Alternatively, an iterative solution can be computed, e.g. by using the conjugate gradient (CG) method on the normal equations of the rewritten Eq. 5 (Hanke and Hansen, 1993; Wagner, 1998), thus avoiding the explicit computation of $(\underline{\underline{C}}^T*\underline{\underline{C}})^{-1}$:

$$minimize\ \Delta = \left\| \begin{bmatrix} \underline{\underline{W}}\ \underline{\underline{M}} \\ 0 \end{bmatrix} + \begin{bmatrix} -\underline{\underline{W}}\ \underline{\underline{L}} \\ \lambda\underline{\underline{C}} \end{bmatrix} \underline{j} \right\|_2^2 \qquad (14)$$

Nonlinear Methods

As soon as one of the m, n, p, or q is not equal to 2, no closed formulation of a solution of Eq. 3 is possible, and nonlinear minimization methods have to be used (Matsuura and Okabe, 1995, 1997). We will concentrate here on the special case with $m=n=p=q=1$, that is the "pure" L_1-norm case. So the task is to

$$\begin{aligned} minimize\ \Delta &= \|\underline{\underline{W}}*(\underline{\underline{M}} - \underline{\underline{L}}*\underline{j})\|_1 + \lambda*\|\underline{\underline{C}}*\underline{j}\|_1 \\ &= \left\| \begin{bmatrix} \underline{\underline{W}}\ \underline{\underline{M}} \\ 0 \end{bmatrix} + \begin{bmatrix} -\underline{\underline{W}}\ \underline{\underline{L}} \\ \lambda\underline{\underline{C}} \end{bmatrix} \underline{j} \right\|_1 \end{aligned} \qquad (15)$$

$$with \quad \|\underline{\underline{A}}\|_1 = \sum_{i=1}^{u} \sum_{k=1}^{v} |a_{ik}|. \qquad (16)$$

Two different algorithms are used for optimization. First, the iteratively reweighted least squares (IRLS) method (Scales et al., 1988; Wagner, 1998) can be used. With this method, an expression

$$\begin{aligned} \Delta &= \|\underline{\underline{A}}*\underline{x} - \underline{y})\|_p^p \\ &= \|\underline{\underline{R}}*(\underline{\underline{A}}*\underline{x} - \underline{y})\|_2^2 \quad with \\ \underline{\underline{R}} &= \mathrm{diag}(|\underline{\underline{A}}*\underline{x} - \underline{y}|^{p/2-1}) \end{aligned} \qquad (17)$$

is minimized by setting $\underline{\underline{R}}_0=\underline{\underline{1}}$ and iteratively determining $\underline{\underline{R}}_i$ from the result of the previous solution, which can again be computed using CG methods.

A second option is the use of linear programming techniques (Luenberger, 1984). This is made possible by introducing vectors of non-negative components $\underline{j}^+$, $\underline{j}^-$, $\underline{e}^+$, and $\underline{e}^-$ of currents and errors such that (Köhler, 1998; Wagner, 1998)

$$\underline{j} = \underline{j}^+ - \underline{j}^- \ and\ \underline{e} = \underline{e}^+ - \underline{e}^- = \underline{\underline{W}}*(\underline{\underline{M}} - \underline{\underline{L}}*\underline{j}). \qquad (18)$$

For diagonal $\underline{\underline{C}}$, one can write Eq. 15 as a sum of terms that depend linearly on the unknowns and that can be minimized using linear programming.

$$\begin{aligned} \Delta &= \|\underline{\underline{W}}*(\underline{\underline{M}} - \underline{\underline{L}}*\underline{j})\|_1 + \lambda*\|\underline{\underline{C}}*\underline{j}\|_1 \\ &= \underline{e}^+ - \underline{e}^- + \lambda*\underline{\underline{C}}*\underline{j}^+ - \lambda*\underline{\underline{C}}*\underline{j}^- \end{aligned} \qquad (19)$$

A formulation for nondiagonal $\underline{\underline{C}}$ can be found in (Wagner, 1998). Advantages of the linear programming framework include the ease of implementing upper bounds on the current densities, i.e. the elements of $\underline{j}^+$ and $\underline{j}^-$, and an elegant option of determining λ which is presented below.

Advantages of both L_1-norm methods are that much more focal current distributions can result and that they are more robust with respect to outliers in the measured data. Both effects have their origin in the fact that large current components j_i or data values m_i are not punished by their squared strengths as in the MNLS case, but contribute with their (weighted) absolute values to the function to be minimized only.

Lead-Field Normalization

To account for the undesired depth dependency of all current density algorithms, a weighting of the current locations or components can be introduced to compensate for different gains and thus achieve an unbiased lead-field distribution. To keep the formulations simple, we will discuss the common case of $c=3$ dipole components only, the special case of $c=2$ for MEG with spherical volume conductor is very similar.

Each column of the lead-field matrix L contains the s sensor responses generated by a unit current component of a dipole located at a certain position. Three orthogonal components at one position describe the effect of all possible dipole orientations at this specific location. The resulting dipole is represented by a linear combination of these three components. Since every orthogonal basis can be used, a component-wise weighting would depend on the choice of this basis. A unique basis can be chosen by using an SVD of the corresponding columns of the lead-field matrix comprising the c dipole components at position i:

$$\underline{\underline{L}}_i = \underline{\underline{U}}_i*\underline{\underline{\Sigma}}_i*\underline{\underline{V}}_i^T \qquad (20)$$

The ortho-normalized sensor responses or field patterns are contained in columns of matrix $\underline{\underline{U}}_i$, the corresponding gains or system sensitivities are the elements of the diagonal matrix $\underline{\underline{\Sigma}}_i$, and the new ortho-normal basis vectors can be found in matrix $\underline{\underline{V}}_i^T$. The elements σ_{ij} of

the diagonal gain matrix $\underline{\underline{\Sigma}}_i$ can now be used to compensate for the depth dependency. If a location-wise normalization is performed, the inverse of the RMS gain

$$g_i = \sqrt{\frac{1}{c}\sum_{j=1}^{c}\sigma_{ij}^2} \quad (21)$$

can be used in the diagonal weighting matrix $\underline{\underline{C}}$ (Eq. 2). For a components-wise weighting, that can also account for the different gains of the different components, e.g. the low gain quasi-radial components in a BEM-model for MEG (Fuchs et al., 1998*a*,*b*), the inverted component gains σ_{ij} can be used directly. Care has to be taken for very small gain components to not overemphasize these components (e.g., a regularized weighting should be performed [Fuchs et al., 1994*b*]).

If the gain factors are applied directly to compensate the depth dependency of the lead-field gains, a bias-free lead-field matrix ($\underline{\underline{L}}^*\underline{\underline{C}}^{-1}$) is used, for example, in Eq. 11. The remaining term $\underline{\underline{C}}^{-1}$ for the reconstructed current components will lead to an overcompensation and thus overemphasize deep source locations. This effect can be reduced by using square root of the gains in Eq. 21, e.g., for component-wise compensation (Köhler, 1998), weight with (c_{kk}: diagonal elements of $\underline{\underline{C}}$):

$$c_{kk} = 1/\sqrt{\sigma_{ij}} \quad (22)$$

The different depth-weighting approaches will be studied by the simulations. For the nonlinear L_1-norm approaches the full gain compensation method ($c_{kk} = 1/\sigma_{ij}$) is used (Matsuura and Okabe, 1996; Köhler, 1998).

Regularization

The regularization parameter λ is, in principle, a free parameter. Nevertheless, various techniques have been proposed for finding its optimum value, such as generalized cross-validation (Hanke and Hansen, 1993) and the L-curve method (Hansen, 1992). Our Ansatz is motivated by the insight, that the solution should not explain more of the data than is above the noise level (Morozov, 1968), i.e.

$$\|\underline{M} - \underline{\underline{L}}^*\underline{j}\|_2 \cong s/SNR \text{ or } \|\underline{\underline{W}}^*(\underline{M} - \underline{\underline{L}}^*\underline{j})\|_2 \cong s. \quad (23)$$

This goal can be used to iteratively refine the value of λ making use of the fact that there is a monotonous dependency between the data term D and λ. Depending on the method used for solving Eq. 11, it is possible to determine the value of D for a given λ with less computational effort than needed to compute $\underline{j}$ (Köhler, 1998).

When using linear programming techniques and demanding, in the same spirit, that $D=a^*s$, with a in the order of 1, the resulting linear programming problem is

$$\Delta = \underline{\underline{C}}^*\underline{j}^+ - \underline{\underline{C}}^*\underline{j}^-$$

$$\textit{under the constraint that } \|\underline{e}^+ - \underline{e}^-\|_1 = a^*s \quad (24)$$

No iterations are needed to determine λ.

Simulations

To study and compare the different linear and nonlinear current density reconstruction methods and different lead-field normalization weights, simulations with well-defined volume conductor geometry and given test-dipole positions are performed. For computational efficiency an analytically solvable, three spherical shells volume conductor model (e.g., de Munck and Peters, 1993) is used (radii: 85, 91, and 98 mm; conductivities: 0.33, 0.0042, and 0.33 1/Ωm). Eighty-one electrodes are placed according to an extended and refined 10/20 system, and 19 test-dipole positions on the vertical z-axis through the common center of the spheres are chosen (z=−30 to 84 mm, −35% to 99% relative eccentricity, Fig. 1). Radial (vertical) and tangential (horizontal) dipoles are used to investigate orientation dependent effects. To understand noise-dominated properties of the different approaches, two levels of white, Gaussian-distributed, zero mean noise are added to the forward calculated potential distributions.

First, noise with a standard deviation of 0.45 nV is used, leading to a signal-to-noise-ratio (SNR) of about 100 for the most superficial dipoles (at z = 84 mm). The dipoles have a constant strength of 1 nAm throughout all experiments, so depth-dependent SNRs are obtained, which decrease to 38% for radial and to 58% of the maximum SNR for tangential dipoles at the center of the volume conductor (z = 0 mm, Fig. 1). To simulate more realistic conditions for the algorithms tested, a second series of experiments is performed with a noise level of 4.5 nV, which leads to a reduction of all SNRs by one order of magnitude.

All current density reconstructions are performed with support points on a regular 3D-grid with 7-mm grid spacing, clipped by the innermost volume conductor sphere (84 mm radius). This leads to 7497 points and thus to a lead-field matrix of size 81 * 22491. No orientational constraints are used. Since the noise levels are well defined in our studies, the regularization parameters are chosen to exactly match the given SNRs, so no overfitting or underfitting of the data can occur.

The depth normalization of the Minimum Norm Least

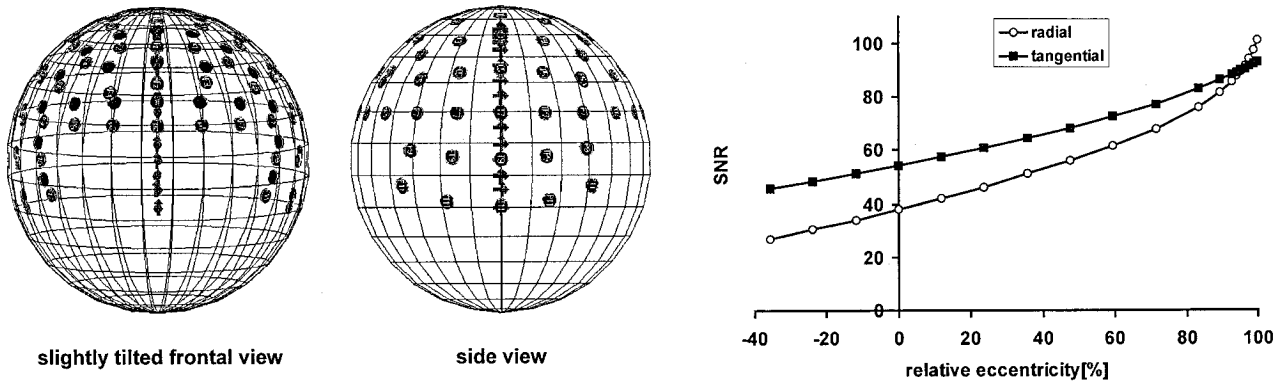

FIG. 1. Slightly tilted frontal (left) and side (middle) view of the set-up used for the simulations. The 81 electrodes are shown as small disks. The outermost shell of the three spherical shells volume conductor model is displayed only. The 19 positions for radially and tangentially oriented test dipoles are indicated by small arrows. Radii/conductivities: 85 mm/0.33 1/Ωm; 91 mm/0.0042 1/Ωm; 98 mm/0.33 1/Ωm. The corresponding signal-to-noise ratios (SNRs) of the simulated dipole fields as a function of the eccentricity relative to the innermost spherical shell radius are shown on the right side. The fixed noise level (0.45 nV) was adjusted to yield SNRs of about 100 for the most superficial test position (z = 84 mm), all dipoles have unit strength (1 nAm).

Squares (MNLS, L_2-norm) and the Laplacian smoothness approaches is performed without (standard implementation for MNLS), with component-wise full (standard for LORETA), and down-weighted powers (square root) of the lead-field gains. The nonlinear L_1-norm methods are calculated with full component-wise normalization weights, which is optimal for these algorithms (Köhler, 1998; Wagner, 1998).

The results are presented as frontal views of a stack of horizontal planes, slightly tilted by 5 degrees. Positions carrying currents below 50% of the largest current (for the linear MNLS and LORETA methods) are clipped to have a better impression of the spatial shape of the reconstructed current densities (full width at half maximum, FWHM). The less blurring, nonlinear methods are differently clipped or displayed: The L_1-CG results are shown clipped at 25% of the maximum current, whereas the L_1-sparse results are visualized by pole symbols scaled by the strengths of the reconstructed currents. All results are shown together with single equivalent dipole fits, that represent (at least in the high SNR series) the generator positions to be reconstructed.

A more quantitative evaluation of the reconstruction results is finally performed by calculating the weighted (by the current strength j_i) centers of the clipped (by a 50% threshold) current distributions for specifying the mislocalizations δr. This is a more adequate method for distributed sources than searching for the maximum current (j_{max}) position and stating its distance to the true source position r_0 only.

$$\Delta r = \|\Sigma j_i * \underline{r}_i / \Sigma j_i - \underline{r}_0\|_2 \quad with \quad j_i > 0.5\, j_{max} \quad (26)$$

The spatial resolution is determined by calculating the FWHM volume, that is all current positions with strengths above 50% of the maximum current are counted and then multiplied by the cell-volume of $7*7*7mm^3 = 0.343cm^3$.

Epileptic Spike Data

The patient data were kindly supplied by Prof. J. Ebersole (Yale, University, New Haven, CT, U.S.A.). Both examinations consist of unaveraged 27 (EEG-1) and 26 (EEG-2) electrode records, measured at 200 Hz sampling rate, the 3D electrode positions, and the 3D positions of three landmarks (Nasion, left and right preauricular points) for registration of the functional data with anatomical image data. The magnetic resonance (MR) data of the first set (EEG-1) are a stack of 124 axial, T_1-weighted, 256 * 256 pixels slices with 2.5-mm slice thickness and a field of view (FOV) of 300 mm. The second anatomic data set consists of 124 coronal slices of the same resolution, a slice thickness of 1.5 mm and a FOV of 220 mm.

Both data sets are analyzed by the linear and nonlinear current density reconstruction methods as described above. Since the individual anatomic data are available, a more realistic volume conductor model is used, and cortical constraints are applied to include physiologic a priori knowledge.

The Boundary Element Method (BEM) volume conductor models are set up from the MR data by segmentation and triangulation of the three main compartments: brain with liquor (inside of the skull), outside of the skull, and outside of the skin (Wagner et al., 1995; Fuchs et al., 1998*a*). Standard conductivity values are used (0.33, 0.0042, and 0.33 1/Ωm) for the three compartments. In the first case (EEG-1) these compartments

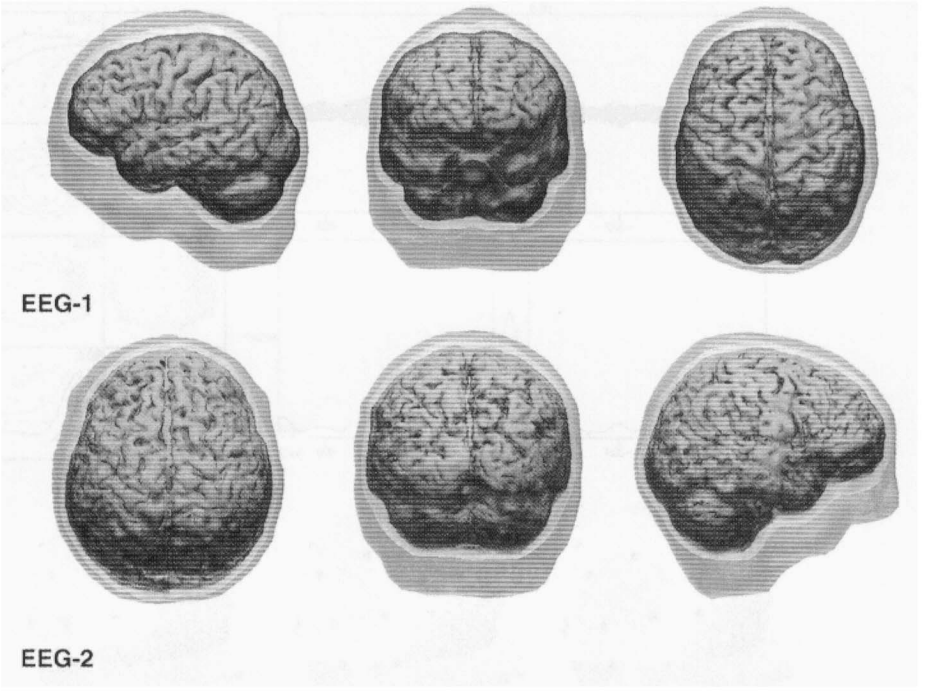

FIG. 2. Boundary element method models for the two epileptic spike data evaluations. Three compartments are segmented from the magnetic resonance images and shown together with the cortical gray matter layer surface, which is used for cortically constrained reconstructions. From left to right: upper row: EEG-1 (4448 nodes/8884 triangles) left, frontal, and top view; lower row: EEG-2 (3907 nodes/7802 triangles) top, rear, and right view.

consist of 1828 nodes/3652 triangles (mean edge length 8.6 mm) for the brain, 1354/2704 (10.6 mm) for the skull, and 1266/2528 (12.5 mm) for the skin. Thus, the model contains 4448 nodes or 8884 triangles in total. The electric potential dependency over the triangles is approximated to be constant on virtually refined, planar subtriangles (Fuchs et al., 1998*a*). To improve the models, the so-called isolated problem approach (IPA) (Hämäläinen and Sarvas, 1989) is used for the innermost compartments. The set-up for this model takes 300 seconds for solid angle calculation and 600 seconds for the BEM-matrix decomposition (24 seconds for the 1828^2 IPA-matrix) with a standard Intel Pentium II, 400MHz, 256MB RAM computer. For the EEG-2 case the following model is used: brain: 1687 nodes/3370 triangles (7.5 mm), skull: 1197/2390 (9.4 mm), skin 1023/2042 (11.3 mm), total: 3907 nodes/7802 triangles; model set-up times in this case: 230 seconds for solid angle matrix and 435 seconds for matrix decomposition (19 seconds for the 1687^2 IPA-matrix). Figure 2 shows both BEM-models together with the segmented cortical surfaces (Wagner et al., 1995) that are used for overlay with the reconstructed currents and for cortically constrained algorithms.

Current density reconstructions for both studies are performed on regular 3D-grids (7-mm distances) constrained to the inside of the innermost BEM-compartment, leading to 8739 support points for the first data set and 5340 points for the second. The cortical gray matter layers are segmented from the MR-images and thinned to give mean 3D-distances between the remaining nodes of 3.8 mm and 5.7 mm for EEG-1 (24,977 respectively, 9956 points), and 3.6 mm and 5.2 mm for EEG-2 (25,660 respectively, 11,202 points). The cortex normals are also calculated and used for additional orientation constraints.

Both measured EEG-data sets are displayed in Figs. 3 and 4. Potential maps of the latency ranges selected for source reconstructions (EEG-1: −15 to 60 milliseconds [ms], EEG-2: −55 to 20 ms) are shown as isopotential contour lines in spherical projections and projected to the skin-surfaces from the segmented MRIs together with the electrodes. First preanalyses of the chosen reconstruction time ranges, which contain the epileptic spike activities, are shown in Fig. 5. Principal components analyses (PCA) are performed by singular value decomposition (SVD) and the dominating three field patterns are displayed together with their temporal loadings (amplitudes) and their overall weights. An SNR normalization is performed (Fuchs et al., 1998*b*), to reveal the number of relevant patterns, which corresponds to the number of fixed current distributions needed to explain the measured data. The noise of the first data set is estimated from prespike latencies (−500 to −125 ms, 13 μV) resulting in a maximum SNR of 15 at 25 ms, in the second case an average noise of 10 μV is estimated, which yields a maximum SNR of 11 at 0 ms. For the EEG-1-data two patterns exhibit an SNR above 1, whereas for the second data-set three patterns are above

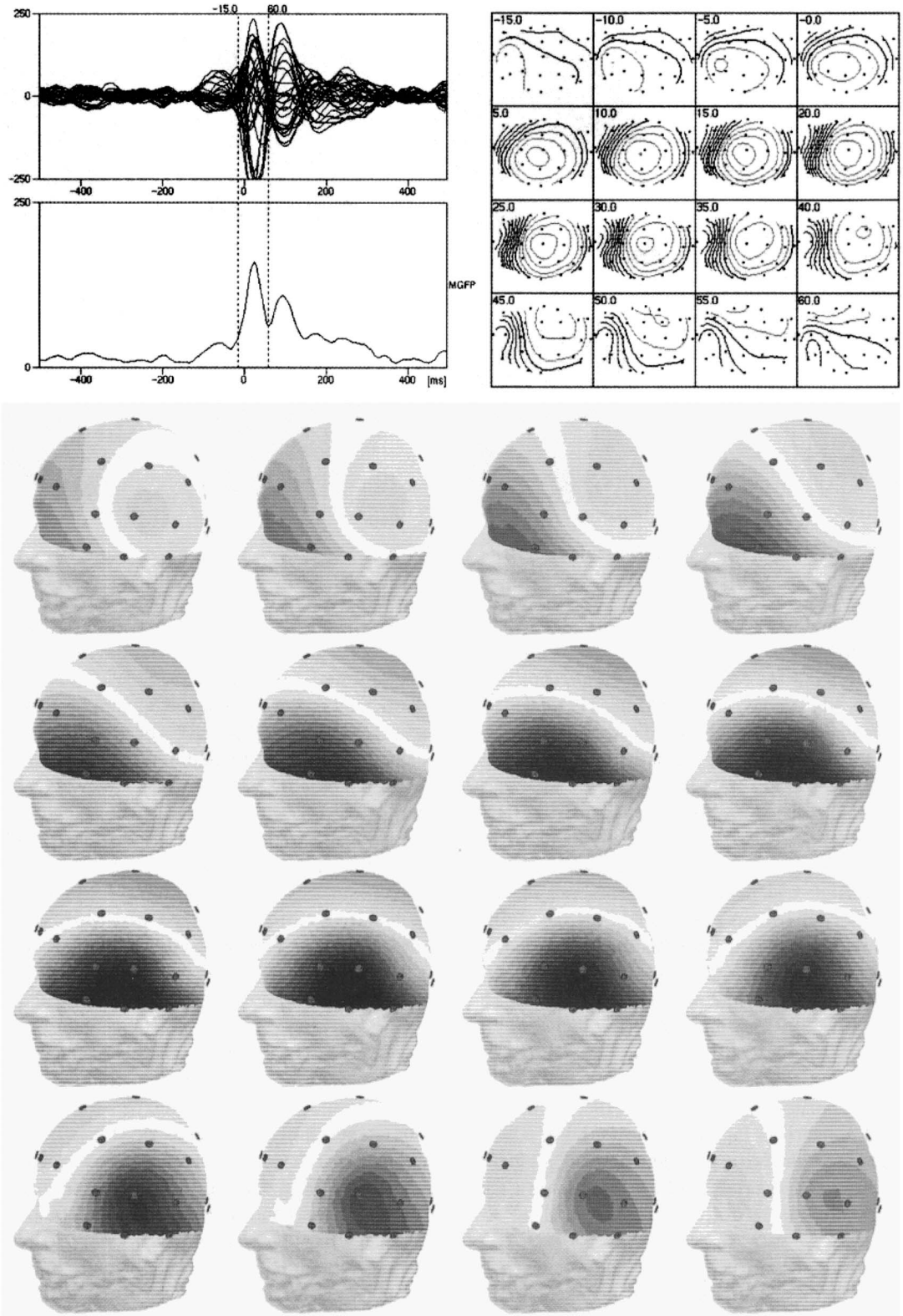

FIG. 3. Epileptic spike data set 1 measured at 200 Hz sampling rate. Upper left corner: butterfly plot and mean global field power (MGFP, lower trace) of the 27 electrode signals; upper right: isopotential contour lines as spherical projections (top view) of the selected time range around the spike latency (−15 to 60 milliseconds [ms]); lower part: three-dimensional potential maps on the skin segmented from magnetic resonance images together with electrodes seen from the left frontal side of the subject.

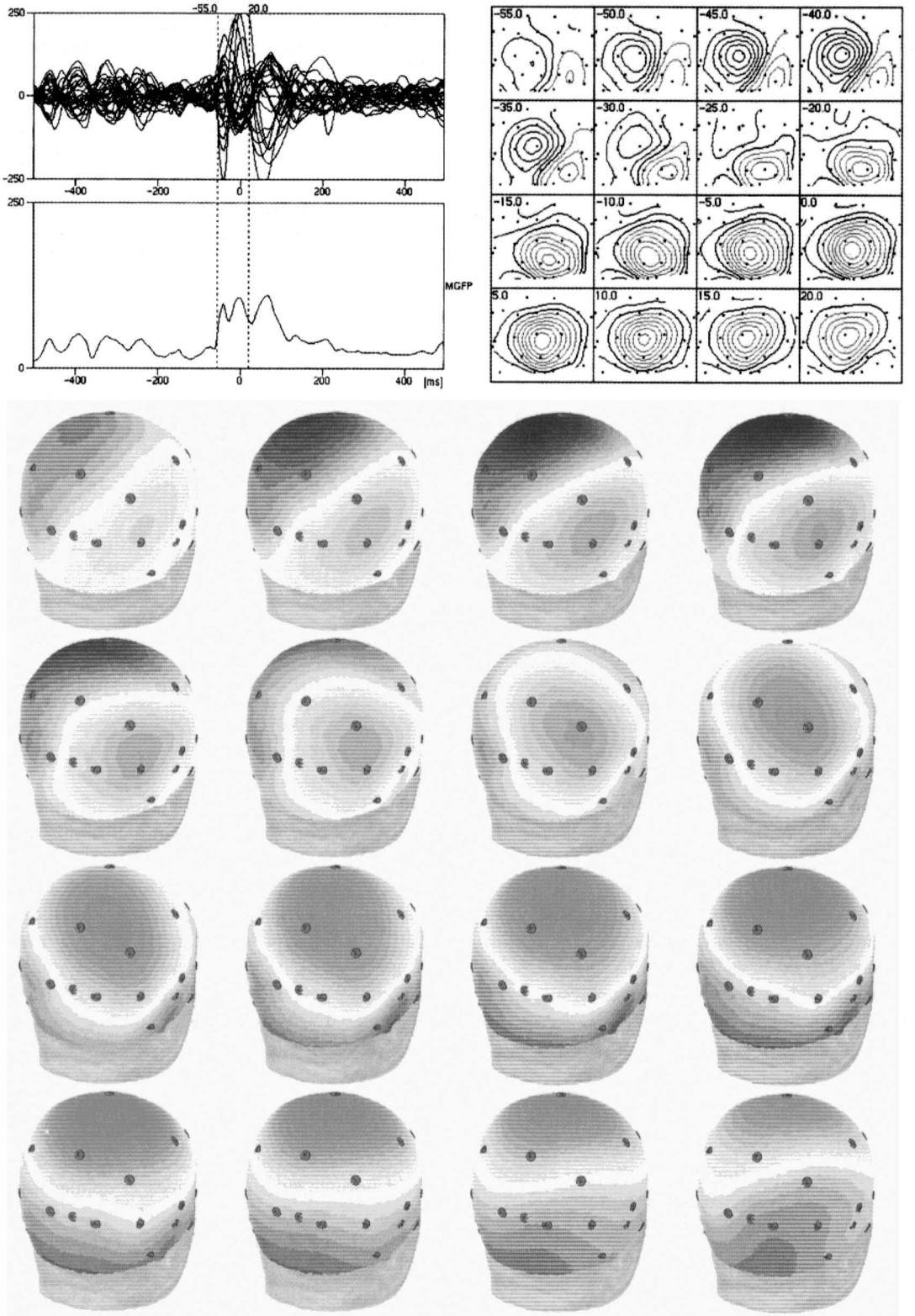

FIG. 4. As Fig. 3 for EEG data set 2. The potential maps (26 electrodes, −55 to 20 milliseconds [ms]) in the lower part of the figure are seen from the upper right back of the subject, MGFP, mean global field power.

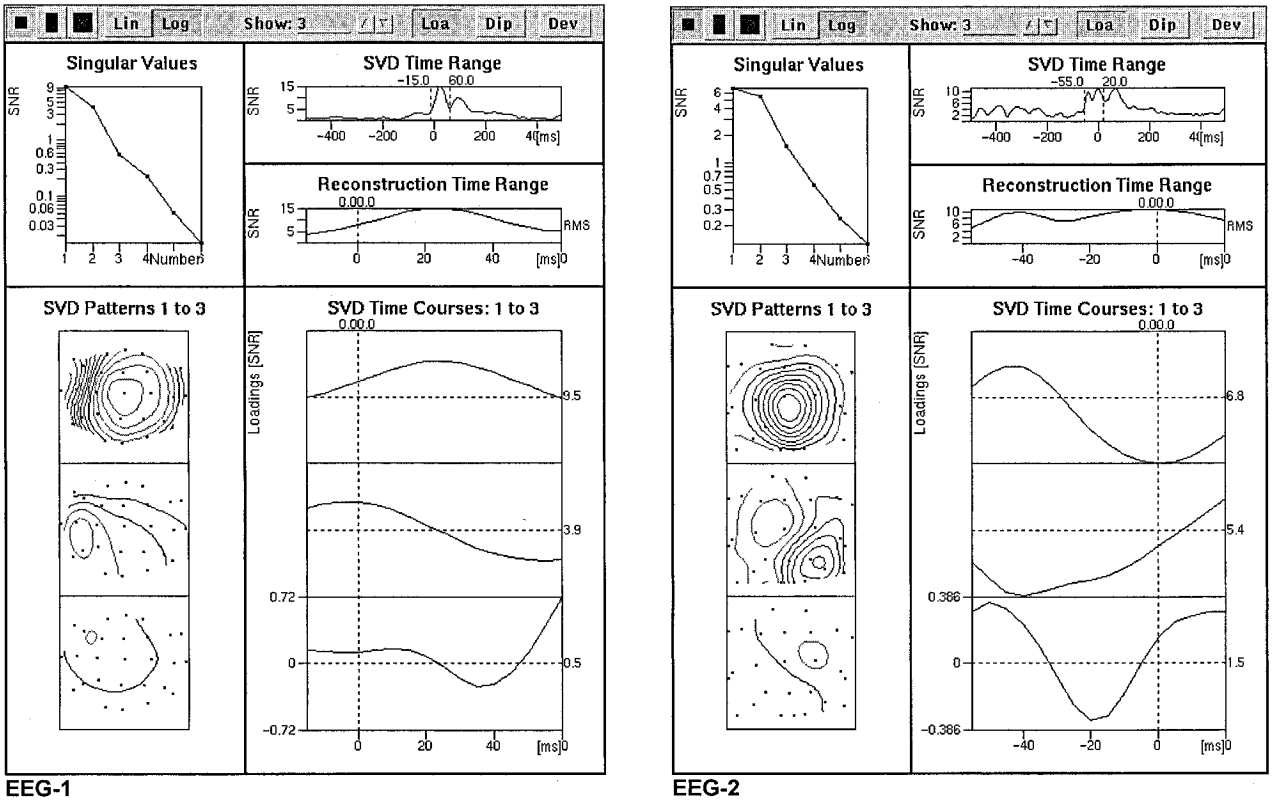

FIG. 5. Principal component analyses of both epileptic spike measurements. The noise-normalized weights of the three largest patterns are shown in the upper left corners above the corresponding patterns. Their temporal loadings are displayed in the lower right corners. For the first data set (left side, EEG-1) the latency range from −15 to 60 milliseconds [ms] is analyzed, for the second data set (right side, EEG-2) the time range is −55 to 20 ms. Two (EEG-1) respectively three (EEG-2) patterns exhibit signal-to-noise ratios above 1. SVD, singular value decomposition.

this level. So in both cases it is obvious (as can of course already be seen from the temporal dynamics of the corresponding mappings in Figs. 3 and 4), that more than one generator is responsible for the signals in the time ranges of interest.

All simulations and all evaluations of the epileptic spike data were performed with the CURRY V3 software package for multimodal neuroelectromagnetic source reconstruction. (Neuroscan, Sterling, VA, U.S.A.). All electric potential data are common average referenced.

RESULTS

First, the results obtained from the simulated data are presented followed by the findings for the first epileptic spike data evaluation. Lastly, results are presented from the same methods being applied to the second data set.

Simulations

Four groups of simulated data are evaluated: radially and tangentially oriented test dipoles at two different SNR levels each. The high SNR examinations allow the general properties of the different linear and nonlinear current density reconstruction algorithms to be studied under idealized conditions, whereas the second series shows the performance of the methods for more realistic SNRs typical for measured data. The 3D current distributions are displayed as stacks of horizontal planes. Slightly tilted frontal views (compare Fig. 1) are presented to get an impression of spatial resolution and characteristic localization properties of the different methods.

Linear Methods

First, the standard MNLS method with different lead-field normalization techniques is applied to radial and tangential test dipoles at certain depths. Figure 6 shows the results for the high SNR case. For source positions at large eccentricities, relatively small, but too superficially localized distributions, are reconstructed for all depth normalizations used. For deeper sources (relative eccentricities < 50%), the spatial resolution strongly drops until finally, for very deep source positions, all support

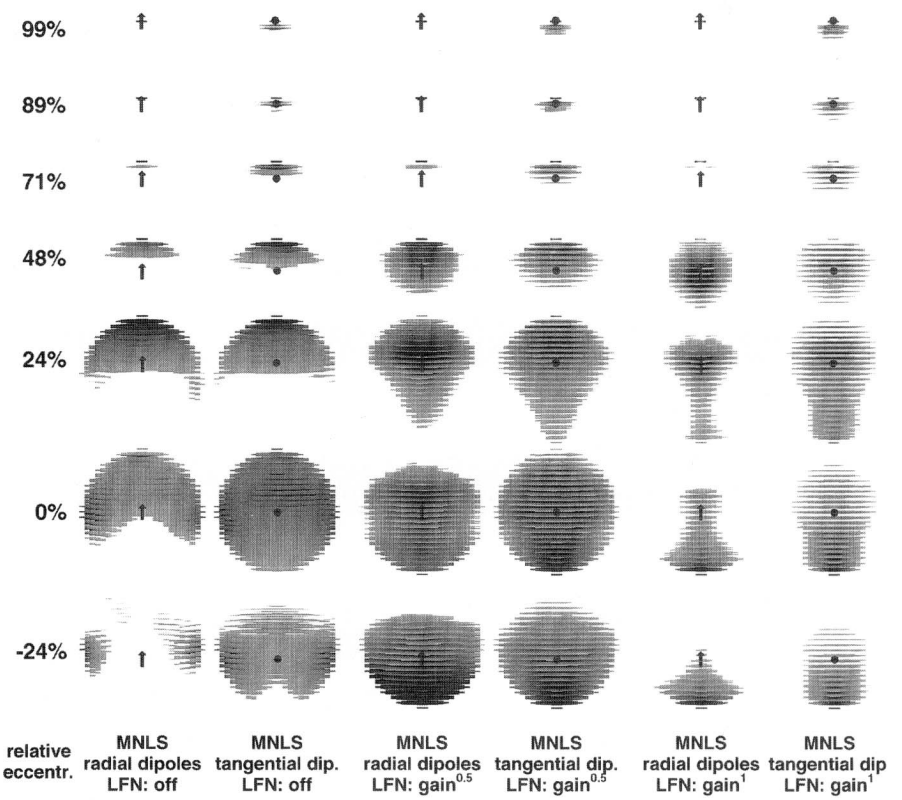

FIG. 6. Minimum norm least squares (MNLS) solutions for radial and tangential test dipoles at different depths (top to bottom rows: 99%, 89%, 71%, 48%, 24%, 0%, −24% relative eccentricity), three spherical shells volume conductor model, 81 electrodes, slightly tilted frontal view to the planes of the three-dimensional reconstruction grid. The current densities are gray level coded and clipped at 50% of the maximum value to visualize the half-width resolution volume. The pairs of columns show different lead-field normalization (LFN) approaches, from left to right: without depth normalization (standard MNLS), with partial ($gain^{0.5}$), and with full depth normalization ($gain^{1}$). The signal-to-noise ratios are smaller than 100 (compare Fig. 1). The true dipole positions are indicated by the centers of the black arrow symbols. dip., dipoles.

points in the volume conductor carry similar (small) currents and the localization of the original source is no longer possible. The results without lead-field normalization are always localized to high, whereas the full-depth normalization overcompensates this effect for the deeper sources (compare Fig. 8). Similar extents and shapes of the current distributions are obtained for radial and tangential test dipole fields.

Figure 7 displays the results for the high SNR data reconstructed by the Laplacian smoothness method (LORETA) together with the reconstructions of the low SNR cases for both MNLS and LORETA with the optimal depth normalization ($gain^{0.5}$) only. Since the Laplacian smoothness approach is, as expected, relatively insensitive to depth normalization, the optimum weighting method is displayed only, the uncompensated and overcompensated cases look very similar and are quantitatively evaluated in Fig. 8 (see below). For the large eccentricities, too deep localizations are found, which is a well-known property of this method: for support points close to the limiting inside of the volume conductor, the 3D smoothness condition is hard to fulfill, because the (virtual) outside neighbors of these points are down-weighted. However, the centers of the nearly spherical current distributions follow the true dipole positions quite nicely for deeper positions and they exhibit better spatial resolutions as compared to the MNLS method. The lower SNR cases (all SNRs are reduced by a factor of 0.1, compare Fig. 1) show similar behavior as the high SNR cases, but more blurred and more irregularly shaped distributions are reconstructed, especially for deeper source locations which exhibit even further reduced SNRs. More quantitative evaluations of the MNLS and LORETA methods are displayed in Fig. 8, where for the high SNR case, all depth normalization approaches are compared with respect to the localization accuracy as a function of the relative eccentricities of the test dipoles. The distances of the weighted (by the reconstructed current strengths) centers of gravity of the clipped (at half maximum values) distributions to the true dipole positions are shown. In all cases the partial depth normalization shows the best overall localization accuracy. The quantitative evaluations of the low SNR cases are shown later, together with the results of the nonlinear methods.

Nonlinear Methods

Figure 9 displays the current density reconstruction results of the nonlinear L_1-norm approaches. Both CG

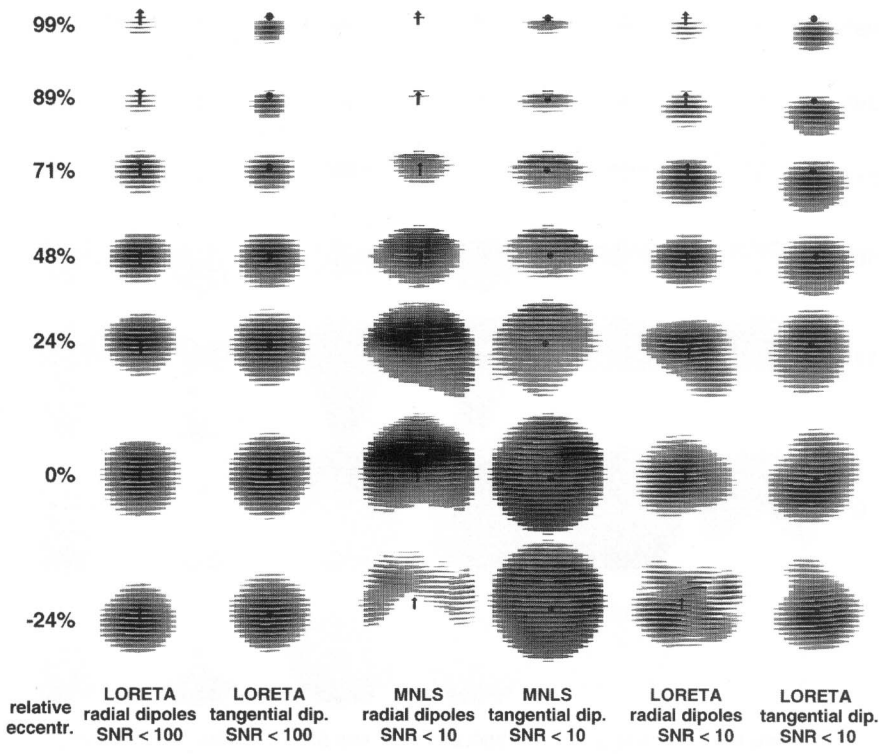

FIG. 7. As Fig. 6, but for Laplacian smoothness reconstructions (LORETA) and for more realistic signal-to-noise ratios (SNRs) below 10. The two left columns show the improved LORETA approach with partial ($gain^{0.5}$) depth normalization for large SNRs (below 100), the middle and right columns display the results for reduced SNRs with the optimum depth normalization for minimum norm least squares (MNLS) and LORETA respectively. dip., dipoles; relative eccentr., relative eccentricity.

minimization and sparse methods are shown for the high SNR cases and more realistic low SNR cases. The CG current distributions are clipped at 25% of the maximum current, whereas the sparse solutions are not clipped, but shown as pole symbols pointing in the directions of the currents and with their base centers at the support point positions. The CG method has relatively small localization errors in the high SNR case at all source positions above the center of the spherical volume conductor, whereas below the center at negative eccentricities the sources are reconstructed to deep (compare Fig. 10). For low SNRs the current distributions are more blurred and irregular shapes result for very deep source positions (relative eccentricities below 20%). In some of the latter cases no currents at all are reconstructed where the original source was, but more superficial, scattered distributions are obtained.

The sparse L_1-norm solutions exhibit the smallest localization errors, except for very deep, low SNR sources, where the reconstructed dipoles begin to scatter and give spurious results.

For a quantitative evaluation of the reconstruction methods presented above, the center positions and the relative (to the innermost spherical shell) volumes of the reconstructed currents with amplitudes larger than 50% of the largest current (full width at half maximum) are calculated. The results are shown in Fig. 10 for the high SNR cases (SNRs below 100) and all four linear and nonlinear approaches. Figure 11 displays the same evaluations for the low SNR cases (SNRs below 10). All 19 test dipole positions are evaluated here, whereas in the graphical figures above selections of seven representative positions are displayed only.

From Figs. 10 and 11 it is obvious, that the Laplacian smoothness approach (LORETA) performs better than the MNLS method. Superficial sources are localized too deep, but the overall accuracy and spatial resolution is superior to the classical MNLS results, where high eccentricity sources are reconstructed at too superficial positions and deeper sources (relative eccentricity $<$ 40%) suffer from bad spatial resolution. Close to the volume conductor center the whole volume "lights up" and all support points carry small currents. LORETA is less sensitive to inadequate lead-field (depth) normalization, since the model term depends only indirectly on the current strength, whereas the MNLS model term directly punishes the squared source strengths and thus this method shows a strong dependency on the choice of the gain compensation approach. With low SNR data both linear methods loose localization accuracy and exhibit slightly decreased spatial resolution.

The nonlinear L_1-norm algorithms perform better than the linear methods at high SNRs: for sources in the upper hemisphere (rel. ecc. $>$ 0%) the maximum relative lo-

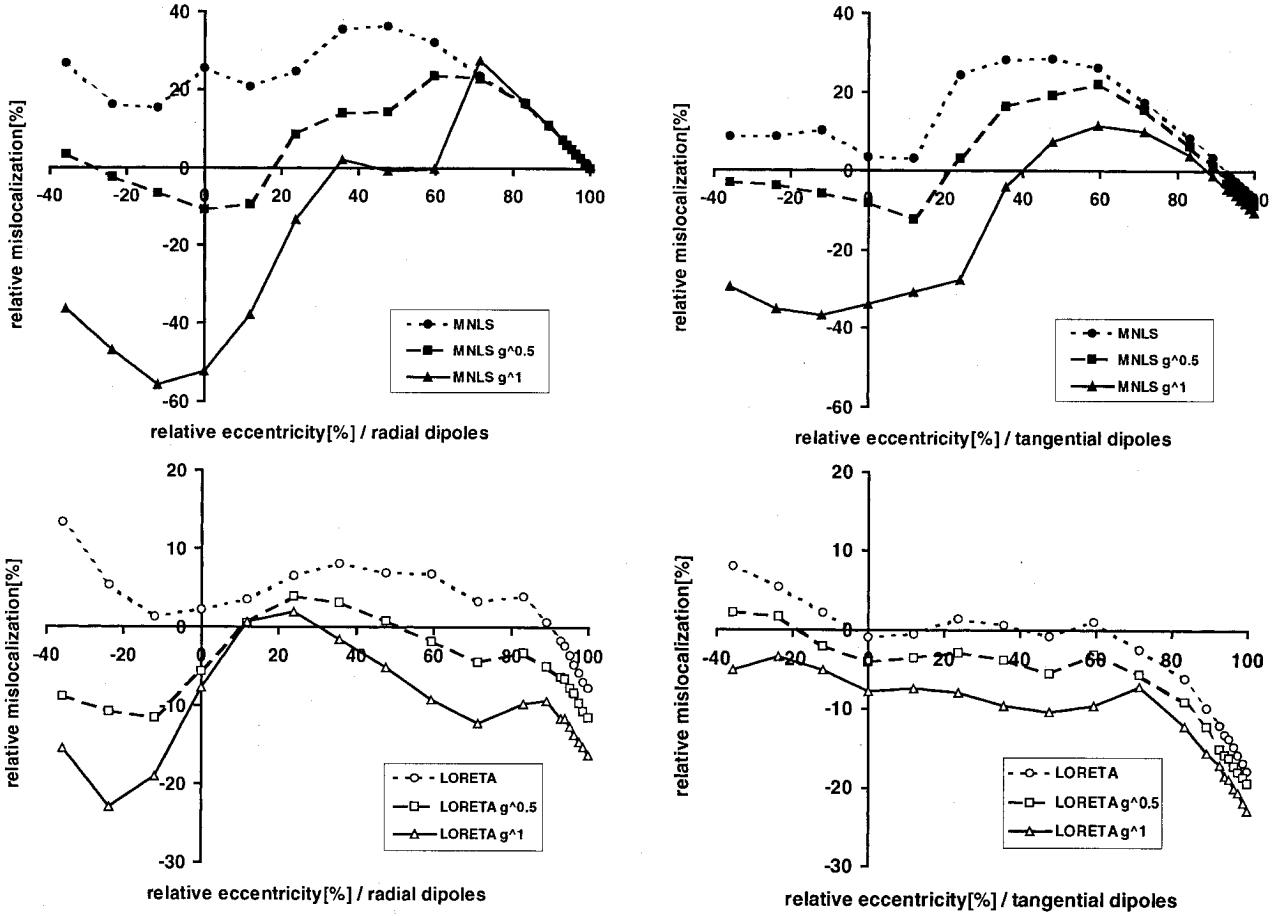

FIG. 8. Quantitative evaluations of the linear minimum norm least squares (MNLS) (upper row) and Laplacian smoothness reconstructions (LORETA) (lower row) methods for radial (left) and tangential (right) test dipoles for different lead-field normalization approaches. The distances of the weighted centers of the current density reconstructions (strengths above 50% of the largest current) to the true test dipole positions are plotted as a function of the relative eccentricity. All distances are normalized to the innermost spherical shell radius.

calization errors are in the order of 10%. The spatial resolution is about a factor of three better for the L_1 CG method compared to LORETA. For the sparse L_1 method the spatial resolution cannot be determined in the same way as for the other approaches, since here the number of active source positions is limited to the number of sensors used.

With low SNR data and deep source positions both nonlinear methods show their limits: scattered results with large mislocalizations and bad spatial resolution can be achieved only. The center of gravity of the largest currents and their volume in these cases are no longer an appropriate measure to quantify the main properties of the results of these algorithms.

Regularization

As mentioned before, all reconstruction results so far are obtained by adjusting the regularization parameter, so that the known SNR of the simulated data is met. Thus no overfitting or underfitting of the data occurred. To study the sensitivity of the different methods with respect to the wrong choice of this essential parameter, the following studies are performed. With real measured data, where in most cases the noise level can only roughly be estimated, these issues are of special importance. Figures 12 and 13 show the stability of all linear and nonlinear approaches for radial and tangential test dipoles at a fixed depth (71% ≅ 60mm) for high and low SNR levels. The regularization parameter is adjusted to give relative deviations to the correct fit quality ranging from 0.1 to 10. In the high SNR cases, all methods are rather uncritical to the choice of the regularization parameter, whereas in the low SNR cases all methods are very sensitive to overfitting the data: scattered distributions or ghost sources appear. Underfitting the data is less critical: the spatial resolution decreases and the centers of distributions of the linear methods slightly shift towards deeper locations, which is caused by the

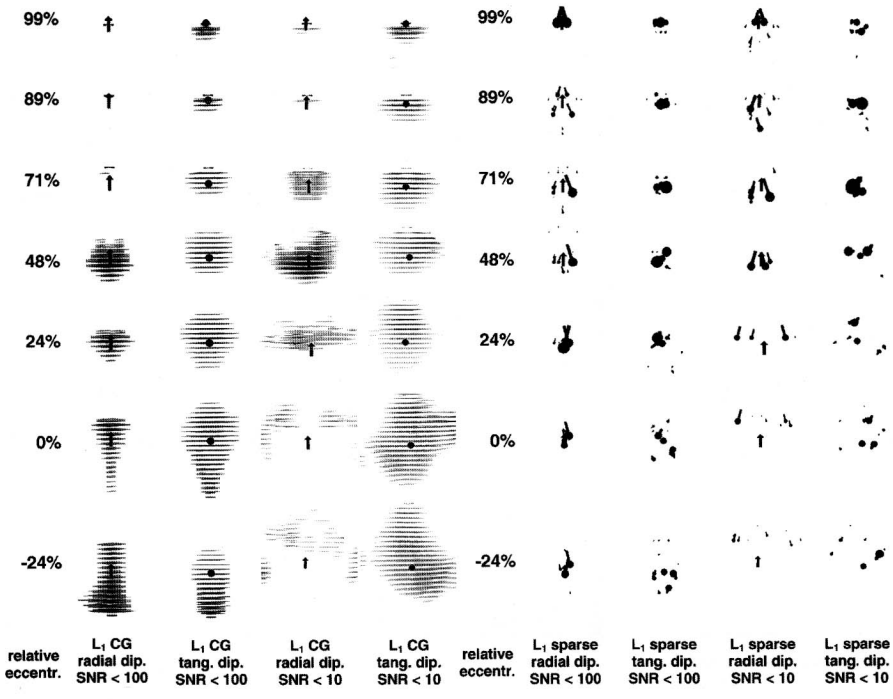

FIG. 9. Nonlinear current density reconstructions (L_1-norm) with conjugate gradient (CG) minimization (left part) and sparse solution algorithm (right part) for radial and tangential test dipoles at both high (left columns) and low (right columns) signal-to-noise ratio (SNR) levels. The CG-results are displayed like the linear method results (clipped > 25%), whereas the sparse L_1-norm results are presented as black pole symbols (test dipole depths as in Fig. 6). radial dip., radial dipole; relative eccentr., relative eccentricity; tang. dip., tangential dipoles.

increasing influence of the model term. With the original, overcompensating (gain[1]) implementation of Laplacian smoothness (LORETA), these effects are even worse. Thus, for real data an appropriate choice of the regularization parameter as a function of the SNR of the measurement is essential.

Unknown Epileptic Spike Data

To have reference reconstruction results for the unknown epileptic spike data sets, standard methods like single equivalent moving dipoles and spatiotemporal dipole models (MUSIC, [Mosher et al., 1992]) are fitted at latency ranges around the spikes of the spike-wave complexes and their results are compared to the current density distributions calculated by the different linear and nonlinear reconstruction methods.

Epileptic Spike Data EEG-1

For the EEG-1 data set single equivalent dipole fits with a three spherical shells volume conductor (common center fitted to the 27 electrodes) are used for comparison with the more realistic BEM model (Fig. 2). Traces of the best fit dipole positions (−15 to 60 ms, compare Figs. 2 and 5) for both volume conductor models are shown in Fig. 14, overlayed onto an enlarged view of the left temporal lobe area of the cortical gray matter layer. Because of the nonspherical shape of the head in the temporal lobe region, the oversimplifying spherical model results in mainly vertically, upwards (2 to 3 cm) shifted dipole positions (Yvert et al., 1997; Fuchs et al., 1998*a*). Lateral and horizontal shifts to posterior locations can also be seen. The qualitative behavior of both reconstruction series is the same: a nearly circular trace of the dipoles, which represent the centers of gravity of the activated cortical patch (de Munck et al., 1988), and similar source orientations (Scherg and Ebersole, 1993), when the SNR is large enough to give stable results. Because the source locations are close to the innermost compartment boundary, the BEM dipoles tend to be slightly more unstable in position and orientation (Fuchs et al., 1998*c*). Both volume conductor models are able to explain the data reasonably well, so the explained variance or deviation (a measure we prefer, since otherwise every meaningful result is between 90 and 99.9% and comparisons to the SNRs, which are field and not power ratios, are more difficult) gives no hint for the large localization errors introduced by the spherical shells approximation. Thus, all following studies are performed using the more realistic BEM models.

The reconstructed epileptic spike activity seems to start (−10 ms) at the basal, frontal part of the left temporal lobe and then evolves with increasing strengths clockwise (as seen from the front) in a slightly backwards and inwards tilted plane. At the maximum signal strength latencies between 20 and 40 ms, the center of activity seems to originate form the central region of the left temporal lobe. The dipole orientations change from

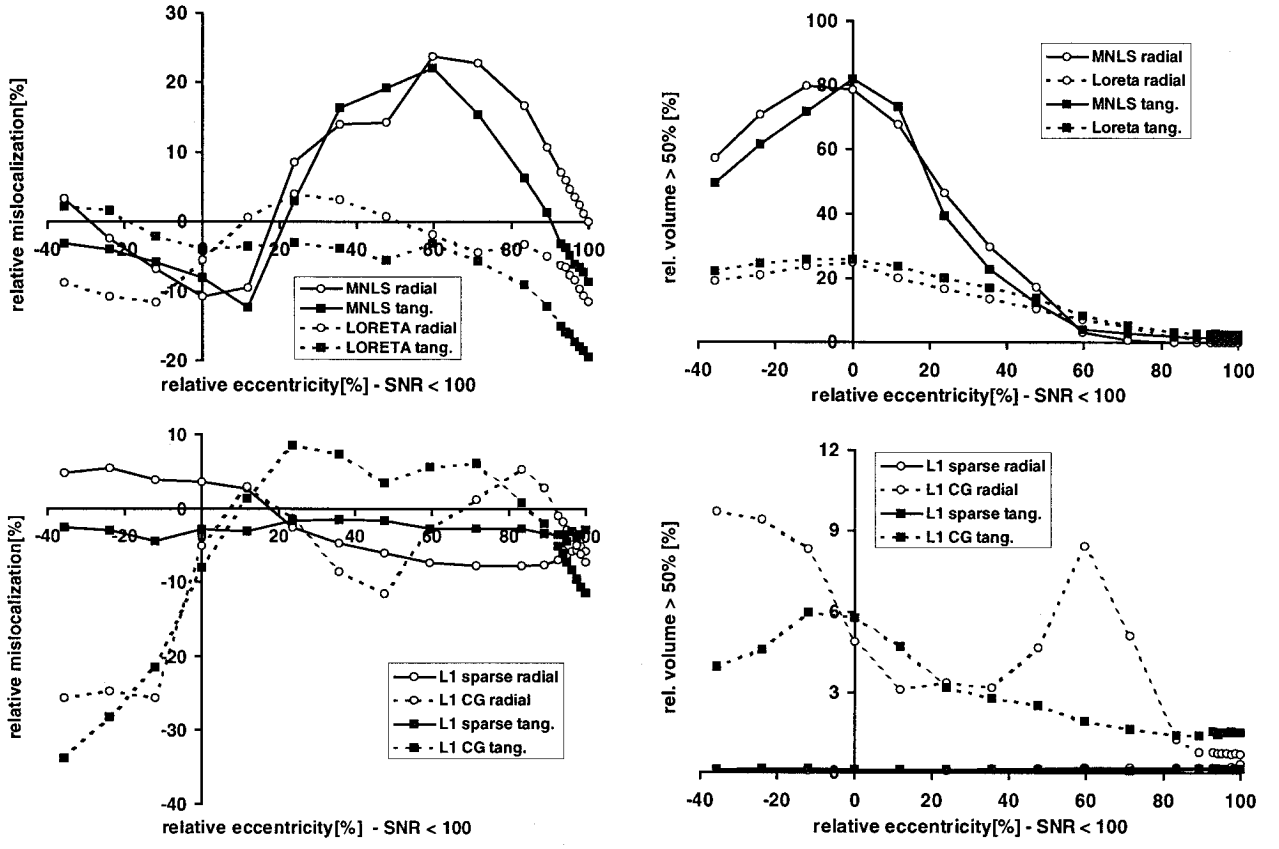

FIG. 10. Quantitative evaluations of localization errors and spatial resolution power of linear (upper row) and nonlinear (lower row) current density reconstruction algorithms at high signal-to-noise ratio (SNR) levels (< 100) as a function of the relative eccentricity of the radial and tangential test dipoles with optimal depth compensation. As in Fig. 8, the thresholded (> 50%) results are used to determine the weighted centers and the full width at half maximum volumes of the reconstructed distributions. The localization errors (left) are normalized to the innermost spherical shell radius, the spatial resolutions (right) are normalized to the volume of this compartment. CG, conjugate gradient; tang., tangential.

pointing backward and upward to a rather vertical inward direction, as can already be expected from the potential maps (Fig. 3).

The spatiotemporal reconstruction results are presented in Fig. 15. Because it is not quite clear from the principal component analysis (Fig. 5) whether the latency range chosen contains two or three relevant patterns, MUSIC fits and scans (Mosher et al., 1992) with two and three fixed dipoles are performed. The dipole reconstructions with the MUSIC metric are performed by an iteratively applied fit (using a multidimensional nonlinear simplex minimizer (Nelder and Mead, 1965)) and projection procedure, very similar to the R-MUSIC approach, published recently by (Mosher and Leahy, 1998). Our implementation will be subject of a future publication. The loadings and the MUSIC scans of the two dipoles fits are shown in Fig. 15. The three dipoles result is also shown (red poles), the third dipole can improve the fit quality slightly, but it is also located at the basal part of the left temporal lobe, so we will continue with the two dipoles case only. The upper dipole loading trace corresponds to the dipole at the basal tip and exhibits a phase reversal, the middle trace belongs to the dipole located in the central region of the left temporal lobe. The lower trace visualizes the explained deviation as a function of time.

MUSIC scans on a 3D grid (5 mm spacing, 24,016 points) and cortically constrained (3.8 mm mean support point distance, 24,977 points) reconstructions without and with surface normals are displayed in the lower part of Fig. 15. All show similar activation of the basal frontal part of the left temporal lobe, without resolving more details, but giving an impression of confidence ranges of the results. Including the surface normals punishes cortical patches with wrong normal orientation, so the result appears more scattered and correctly oriented areas are more emphasized. This approach is nevertheless questionable, because the actual generators are expected to be spread patch-like and to comprise neurons of different orientations.

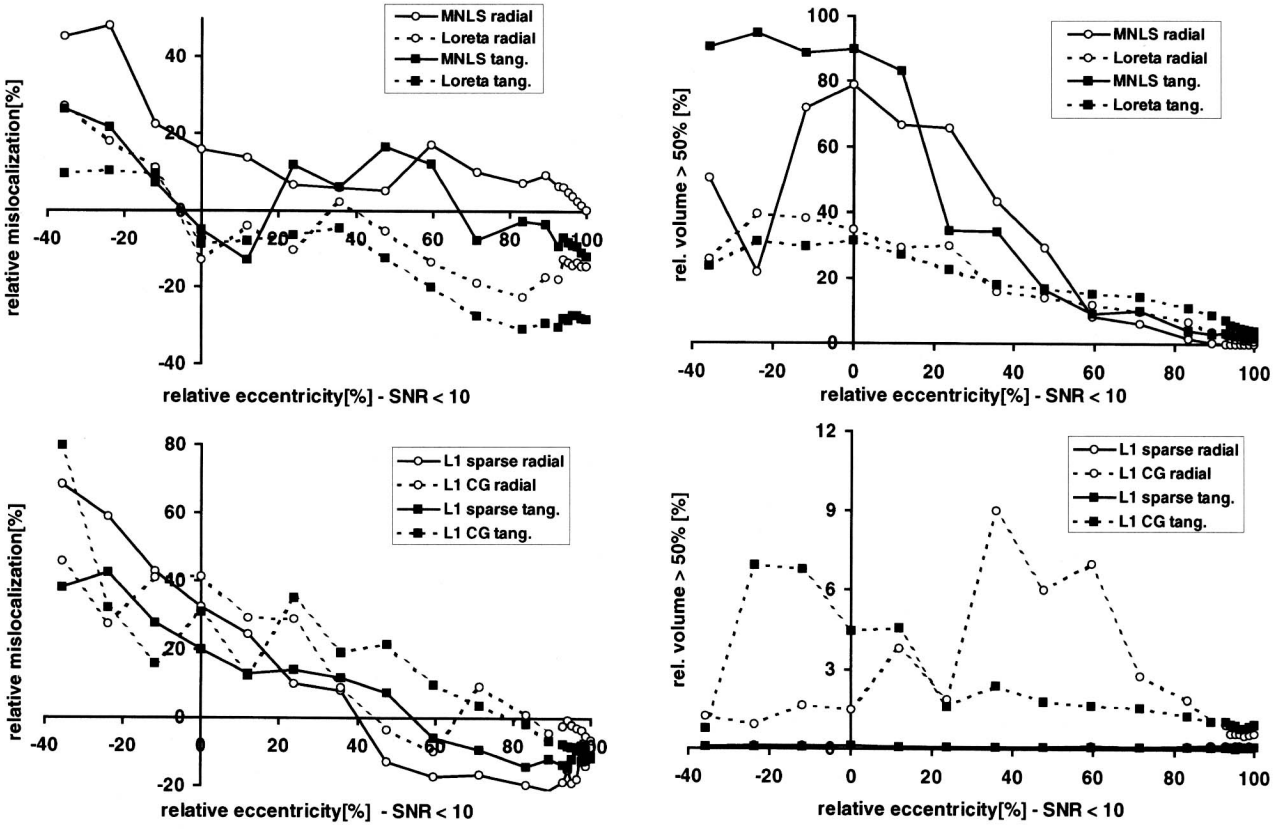

FIG. 11. Same as Fig. 10, but for the low signal-to-noise ratio (SNR) level (< 10) studies. CG, conjugate gradient; Loreta, Laplacian smoothness reconstructions; MNLS, minimum norm least squares; tang., tangential.

Linear and Nonlinear Current Density Reconstructions

The linear current density methods are first applied without cortical constraints, but of course the source space must be limited to the inside of the innermost BEM compartment as before. The results for MNLS, LORETA, L_1-CG, and L_1-sparse methods on regular 3D grids (7 mm spacing, 8739 points) are shown in Fig.

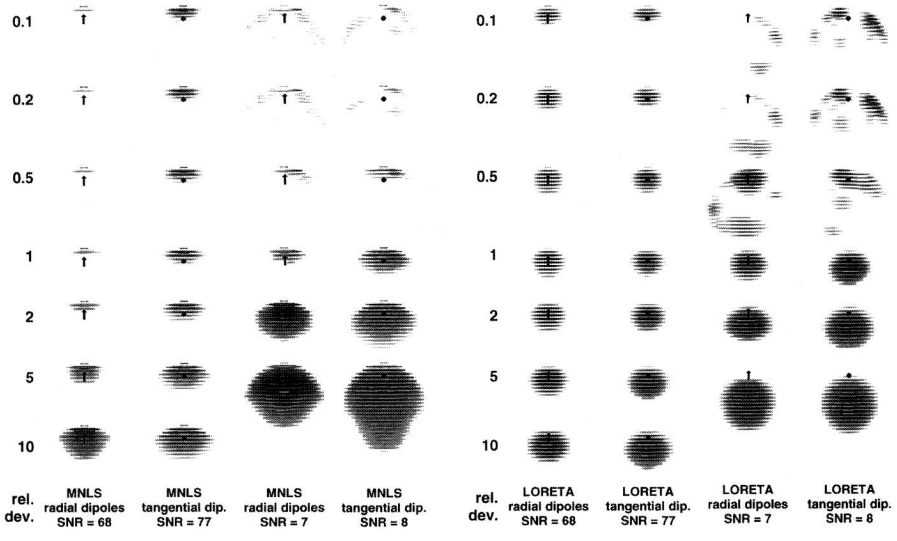

FIG. 12. Linear minimum norm least squares (MNLS) (left columns) and Laplacian smoothness reconstructions (LORETA) (right columns) results for radial and tangential test dipoles at a fixed eccentricity (71% ≅ 60 mm). The regularization parameter, that weights between data and model term, is modified to obtain overfitted and underfitted results. From top to bottom the following factors relative to the correct value for the data-term deviation are adjusted: 0.1, 0.2, 0.5, 1, 2, 5, and 10. Thus, the upper three rows represent overfitted and the lower three rows underfitted data. For the low signal-to-noise ratios (SNR) cases the factor 10 cannot be achieved. dip., dipole; rel dev., relative deviation.

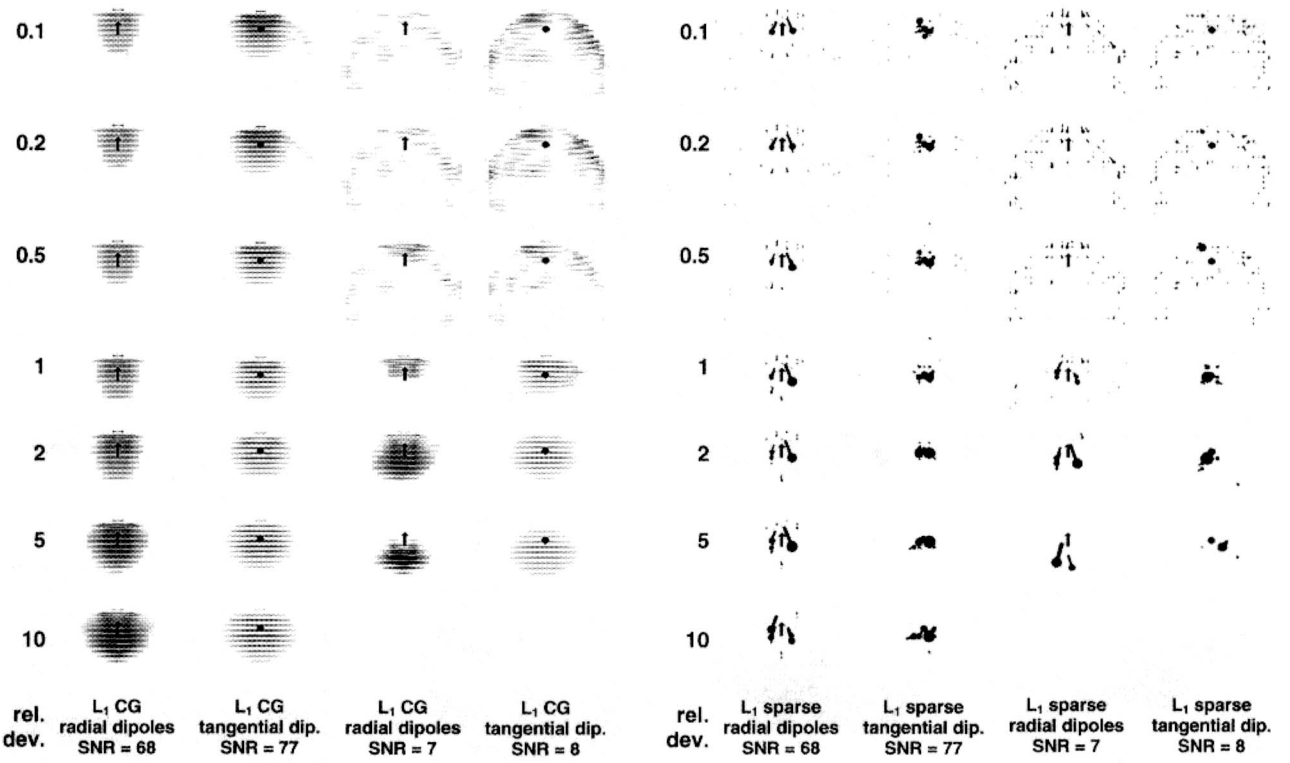

FIG. 13. Same as Fig. 12, but for the nonlinear CG (left columns) and sparse (right columns) L_1-norm algorithms. CG, conjugate gradient; dip., dipole; rel dev., relative deviation; SNR, signal-to-noise ratio.

16 as color coded maps overlayed to the cortical surface for three selected latencies. The results of both linear and the L_1-CG methods are clipped at 50% of the maximum current to give an impression of the spatial resolutions of the different approaches and for better visualization. The spatial resolution is not sufficient to reveal details like the much more focal single dipole models. However, the left temporal lobe area is activated.

As expected from the simulations, MNLS tends to emphasize too superficial source positions, whereas LORETA suppresses activity at these locations and thus results in too deep, blurred current distributions. At later latencies around 20 ms with both linear methods, a

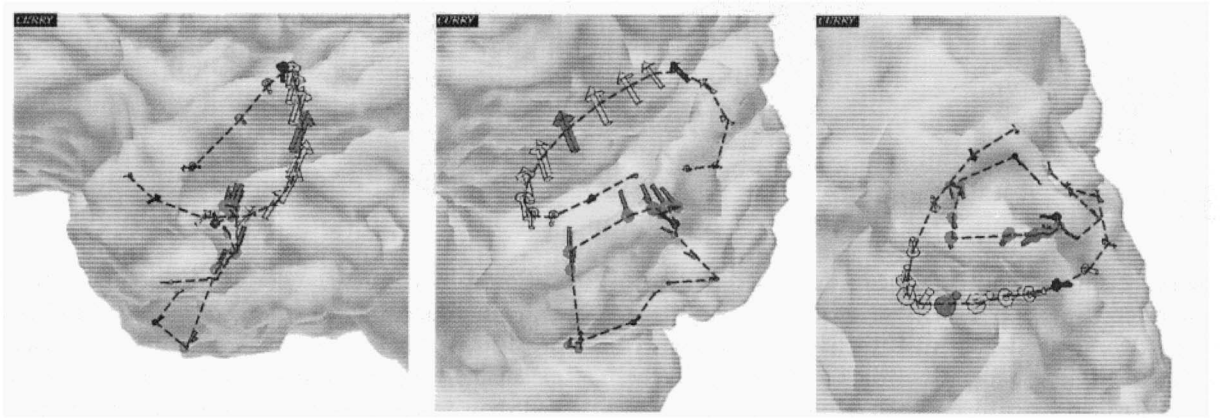

FIG. 14. As reference single moving equivalent dipoles are fitted to EEG-1 epileptic spike data in the latency range from −15 to 60 milliseconds [ms]. Results for a standard three spherical shells volume conductor model (center fitted to the 27 electrodes) (yellow arrows) are compared to a more realistic boundary element method model (Fig. 2, red poles). Enlarged views of the left temporal lobe are shown from left, front, and bottom. Selected latencies for current density reconstructions: −10 ms (black), 20 ms (green), 40 ms (blue).

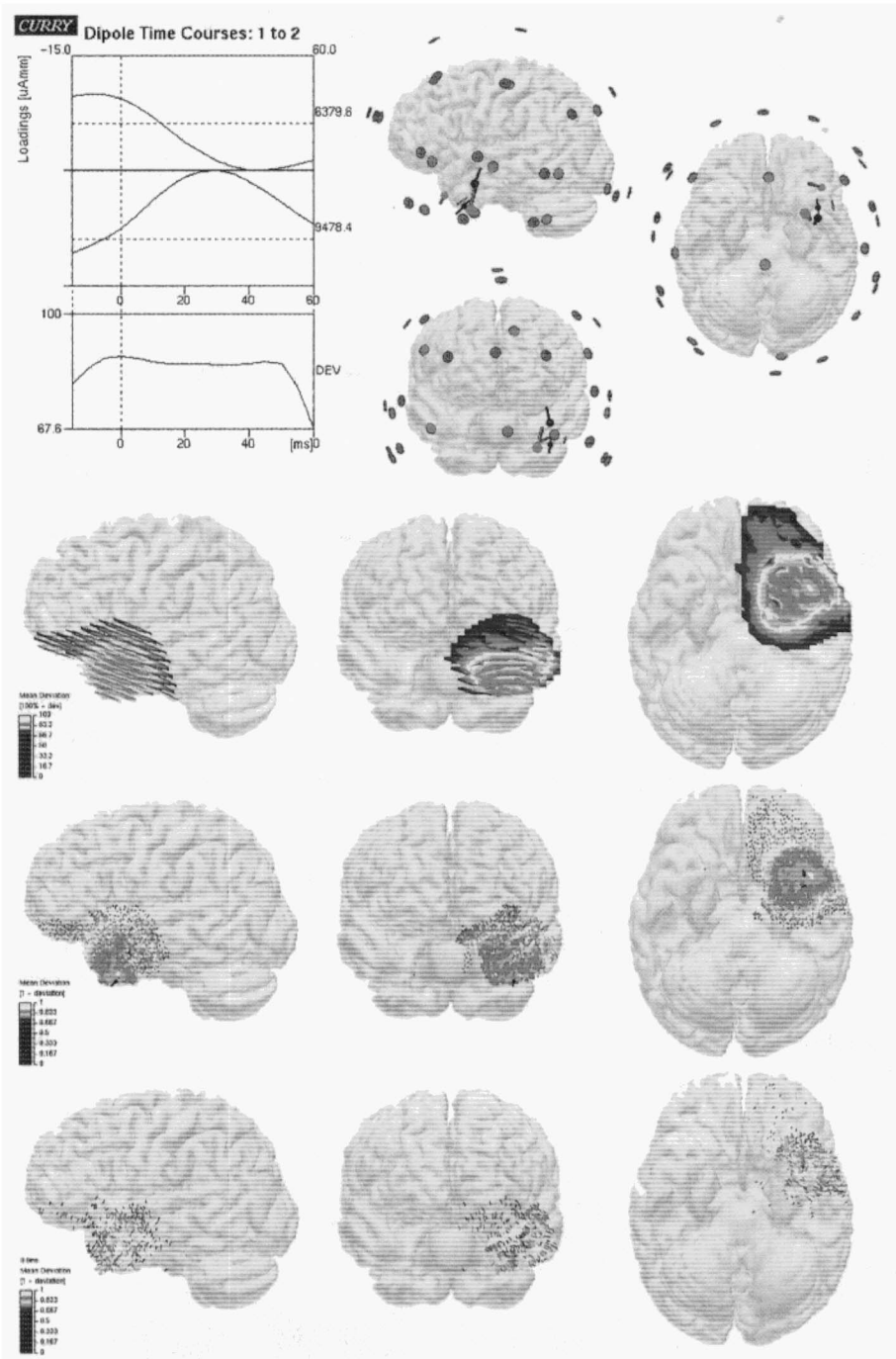

FIG. 15. Spatiotemporal reference reconstructions (EEG-1: −15 to 60 milliseconds [ms]): Dipole fits with MUSIC-metric overlayed to the cortical gray matter layer (upper right): 2 fixed dipoles (black poles), 3 fixed dipoles (red poles). The reconstructed loadings of the two dipoles case are shown in the upper left together with the explained deviation (lower trace) as a function of time. The upper trace corresponds to the dipole at the basal front of the left temporal lobe. The three lower rows show MUSIC scans (2 dipoles) on a three-dimensional grid (5 mm, 24,016 nodes), cortically constrained without (mean node distance: 3.8 mm, 24,977 nodes), and with normals as color coded overlays (all scans clipped > 75%, left to right: left, front, and bottom views).

spread and shift of the reconstructed distributions toward more posterior positions seems to occur, whereas around 40 ms two centers seem to be active simultaneously. Similar behavior is found by the L_1-CG method. The overfocussing L_1 sparse approach results in single or two dominating centers of activity in or around the center of the left temporal lobe and some small outliers, as can be expected from the simulations (Fig. 9).

Cortically constrained current density reconstructions (5.7 mm spacing, 9956 points) of the first EEG data set are displayed in Figs. 17 and 18. All approaches are first calculated without additional surface normal constraints and shown as color coded maps overlayed to the cortical layer, whereas the L_1-sparse results and all methods with normals are presented as current symbols (poles) in Fig. 18. This display option has the advantage, that the

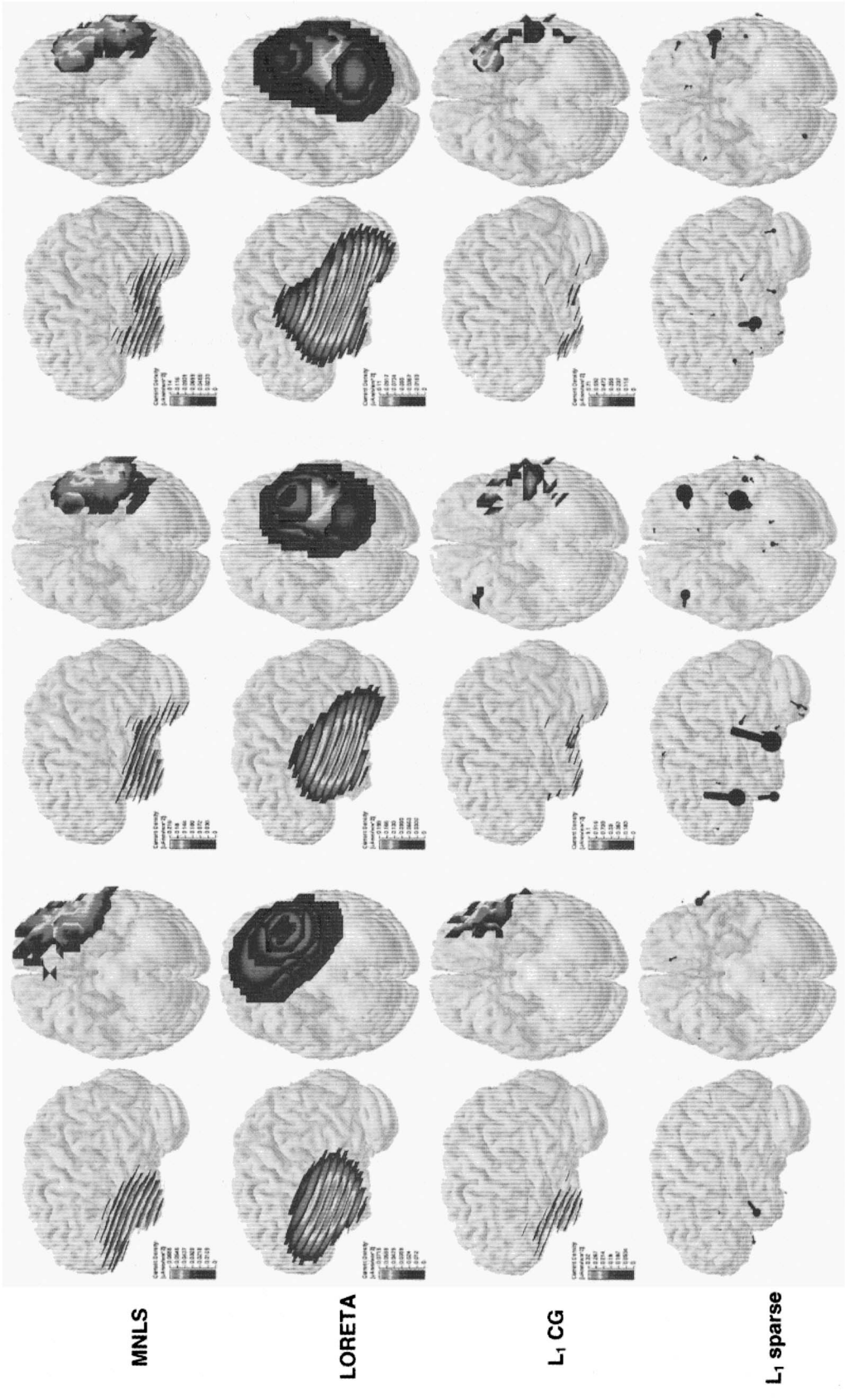

FIG. 16. Linear and nonlinear current density reconstructions (EEG-1) on three-dimensional grids (7 mm, 8739 nodes). Results are displayed together with the cortical gray matter layer in left and bottom views as color coded overlays or poles (L_1 sparse). Top to bottom rows: minimum norm least squares (MNLS), Laplacian smoothness reconstructions (LORETA), L_1 conjugate gradient (CG) (all clipped > 50%), L_1 sparse (50 nAm/mm). Left to right: −10, 20, 40 milliseconds (ms).

important current orientations are also visible. All reconstruction algorithms confirm the findings described above. The Laplacian smoothness approach without cortical surface normals exhibits the worst spatial resolution, the nonlinear methods yield more focal results and the L_1 sparse results seem to be overfocussed. Including orientational constraints results in more focussed distributions, especially for the Laplacian method. Support points with the wrong orientation are suppressed and the remaining cortical surface patches are active only. To insure that the real cortical surface structure is well approximated by the nodes distributed on the cortical gray matter layer and their normals, the thinning radius or mean distance between the nodes should not exceed typical cortical curvature radii.

Epileptic Spike Data EEG-2

Like for the first unknown data set, standard spatio-temporal models are applied to the most interesting latency range around the spike (−55 to 20 ms, Figs. 4 and 5) as reference solution. The results of a three dipoles MUSIC fit and scan are shown in Fig. 19. The spatiotemporal dipole loadings are displayed together with the explained deviations as a function of time. The scan results for a regular 3D grid (5 mm spacing, 14,659 points) and cortically constrained scans (3.6 mm mean distance, 25,660 points) with and without normals can be seen in the lower part of this figure. Furthermore, single equivalent dipoles at two time-points (−40 ms: "tangential" field pattern and 0 ms: "radial" field pattern) are fitted and shown together with the three spatio-temporal dipoles in the upper right. For comparison, a three spherical shells volume conductor model (fitted to the 26 electrodes) is used. In this more favorable case (spherical part of the head) dipole position deviations below 10 mm relative to the BEM model locations are found.

All reconstructed dipoles are located in the upper hemisphere relatively deep below the central sulcus area close to the midline, with the center of gravity slightly shifted to the right side of the brain. At early latencies around −40 ms, the radial components of the posterior dipole and the middle, mainly radially oriented source partly cancel each other to appear as one mainly tangentially oriented generator that can be represented by a single dipole (red pole) as well. At later latencies (around 0 ms) the deep radial source close to the interhemispheric gap pointing to the postcentral gyrus dominates, accompanied by the small anterior source. The middle and the anterior dipole can be resolved by MUSIC scans, whereas the posterior source position is not so obviously visible. However, the reconstructed activated regions of the brain confirm the single equivalent dipole findings. The spatial resolution is limited by the small SNR of the measured data, where "noise" also includes correlated background activity, and not only statistically distributed fluctuations. Unfortunately with single trial data it cannot be distinguished between these different types.

Linear and Nonlinear Current Density Reconstructions

As before, three different classes of support points are used for all distributed source reconstruction algorithms: regular 3D grids (7 mm, 5340 points) and the cortical gray matter layer (5.2 mm, 11,202 points) without and with surface normal constraints. Figures 20, 21, and 22 display the results of these examinations. The linear MNLS and LORETA-like methods exhibit rather blurred current distributions in all cases. The low SNR and the small number of electrodes with rather large interelectrode distances above the reconstructed source areas (compare Fig. 19, top view) show the limits of all approaches in this case. The nonlinear methods reveal rather scattered source patterns, which do not allow further conclusions about the nature of the generators. Again, this behavior can be expected from the low SNR simulations that show similar results even for much more sensors and thus better experimental conditions. The cortically constrained Laplacian smoothness result without normals totally fails to reproduce the outcome of the other methods: blurred, distributed activity far away from the sensors at physiologically not very meaningful areas (cerebellum) is reconstructed in this case. However, this example shows the limitations of source reconstructions caused by the inverse problem, since all results shown are able to explain the measured data. Only a comparison between all possible methods may lead more trustable results, whereas exclusively applied methods, even if they normally work quite well, may fail under some conditions.

Computational Performance

In view of an everyday usage of the algorithms applied and discussed in this article, their computational efforts should not be too demanding. Table 1 presents the performance of the implementations running on a standard high performance PC (Pentium II, 400MHz, 256MB). The set-up and decomposition of the BEM model is of course performed only once (for N nodes the set-up time is proportional to N^2, the time for decomposition $\propto N^3$). The lead-field matrix is also calculated only once per support point set-up (time consumption is linear

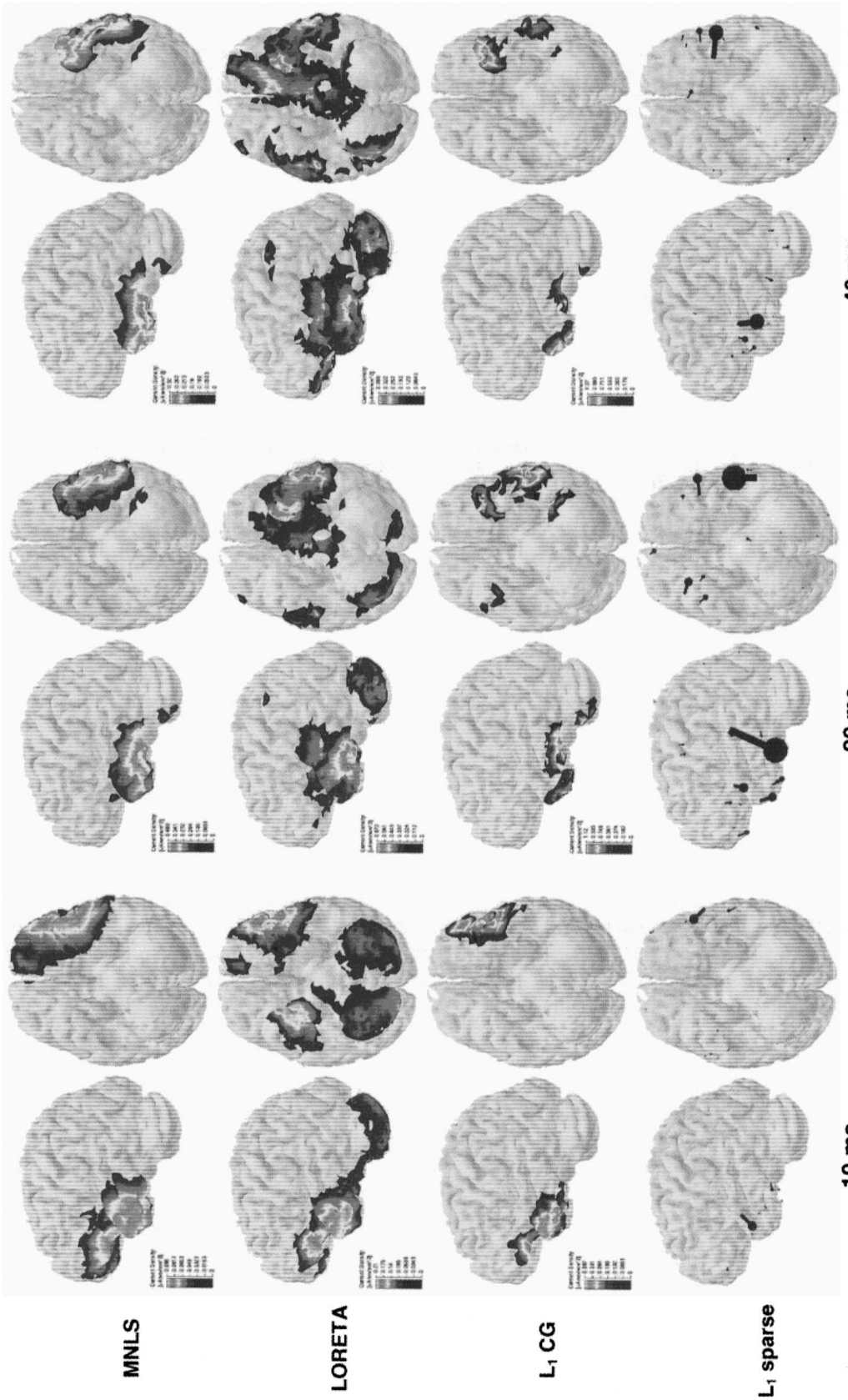

FIG. 17. Cortically constrained current density reconstructions (5.7 mm mean distance, 9956 nodes), without normals. Results are displayed together with the cortical gray matter layer in left and bottom views as color coded overlays or poles (L_1 sparse). Top to bottom rows: minimum norm least squares (MNLS), Laplacian smoothness reconstructions (LORETA), L_1 conjugate gradient (CG) (all clipped > 50%), L_1 sparse (50 nAm/mm). Left to right: −10, 20, 40 milliseconds (ms).

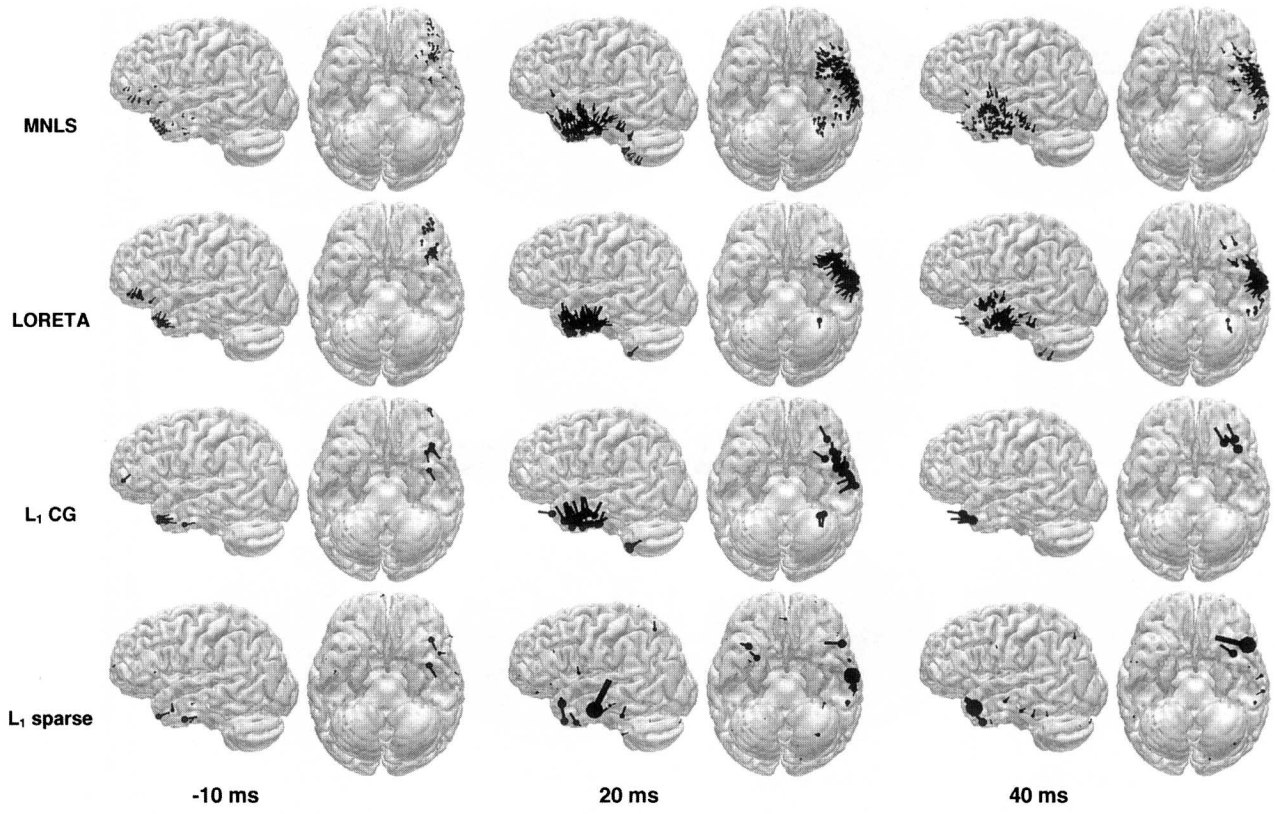

FIG. 18. Similar to Fig. 17, cortically constrained, with normals. Top to bottom rows: minimum norm least squares (MNLS), Laplacian smoothness reconstructions (LORETA), L_1 conjugate gradient (CG) (all clipped > 70%, 1nAm/mm), L_1 sparse (50 nAm/mm). Left to right: −10, 20, 40 millisecond (ms).

in the number of support points). Once the lead-field matrix is calculated, the computational performance no longer depends on the volume conductor model used.

The times needed for the rather demanding CG algorithms used for LORETA and L_1 are one to two orders of magnitude larger than for the linear MNLS approach, whereas the L_1 sparse simplex algorithm needs about twice the time as the Laplacian method. One should keep in mind, that for the latter approach and for L_1 CG several iterations may be needed to achieve an appropriate choice of the regularization parameter. However, all methods can be performed in reasonable times, and thus should be used for comparison and confirmation of other findings (e.g., from spatiotemporal dipole models).

DISCUSSION

Extensive simulations with spherical volume conductor geometry and a large number of electrodes are performed to study the basic properties of different current density reconstruction algorithms with respect to localization accuracy and spatial resolution for the most simple case of single pointlike, dipolar sources. The linear and nonlinear approaches used here are described in detail in the methods section. In the simulations the sensors are distributed according to an extended 10-20 system, and exhibit a rather close spacing and good coverage of the upper hemisphere. Radial and tangential unit strength test-dipoles at 19 different eccentricities are used to evaluate depth and orientation dependencies of the reconstruction methods. Two different signal-to-noise levels are studied: below 100 for idealized conditions, revealing the inherent properties of the approaches, and below 10 for more realistically simulating measured data quality. Support points for the current density reconstructions are chosen on a regular 3D grid limited by the innermost shell of the three spherical shells volume conductor model. Lead-field normalization techniques are tested to find the best compensation method for the undesired tendency of linear and nonlinear minimum norm algorithms to underestimate the source depths. The correct adjustment of the regularization parameter is another important issue studied here.

The partial lead-field compensation gives the best

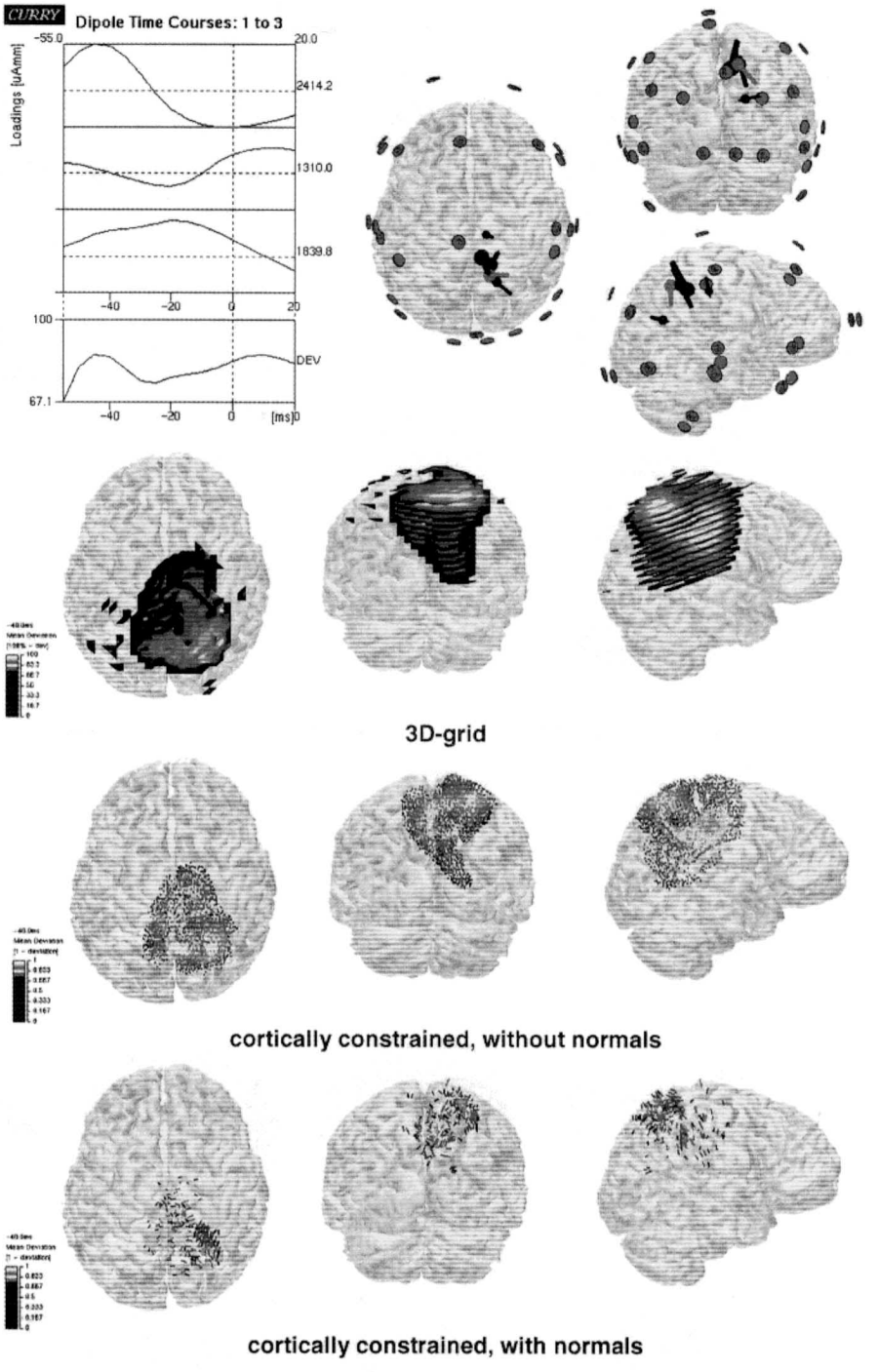

FIG. 19. Similar to Fig. 15, but for EEG-2. Spatiotemporal reference reconstructions (−55 to 20 milliseconds [ms]). Three fixed dipole fits with MUSIC-metric overlayed to the cortical gray matter layer (upper right, black poles). The reconstructed loadings of the three dipoles are shown in the upper left together with the explained deviation (lower trace) as a function of time. Upper trace: middle dipole, second trace: anterior dipole, third trace: posterior dipole. Moving dipole reconstructions at −40 ms (red) and 0 ms (blue) are also shown. The three lower rows show MUSIC scans (3 dipoles) on a three-dimensional grid (5 mm, 14,659 nodes), cortically constrained (3.6 mm, 25,660 nodes) without, and with normals as color coded overlays (all scans clipped > 75%, left to right: top, rear, and right views).

results for the standard Minimum Norm Least Squares and Laplacian smoothness algorithms. However, even with an optimum choice of depth normalization, MNLS underestimates the depth of sources at most eccentricities. The Laplacian smoothness approach (the overcompensated implementation with fixed regularization is known as LORETA (Pascual-Marqui et al., 1995)) at eccentricities above 70% overestimates the source depths, which is due to the smoothness constraint, that cannot be well fulfilled at the source space boundaries. Nevertheless, the modified LORETA method shows the smallest overall localization errors and the best spatial

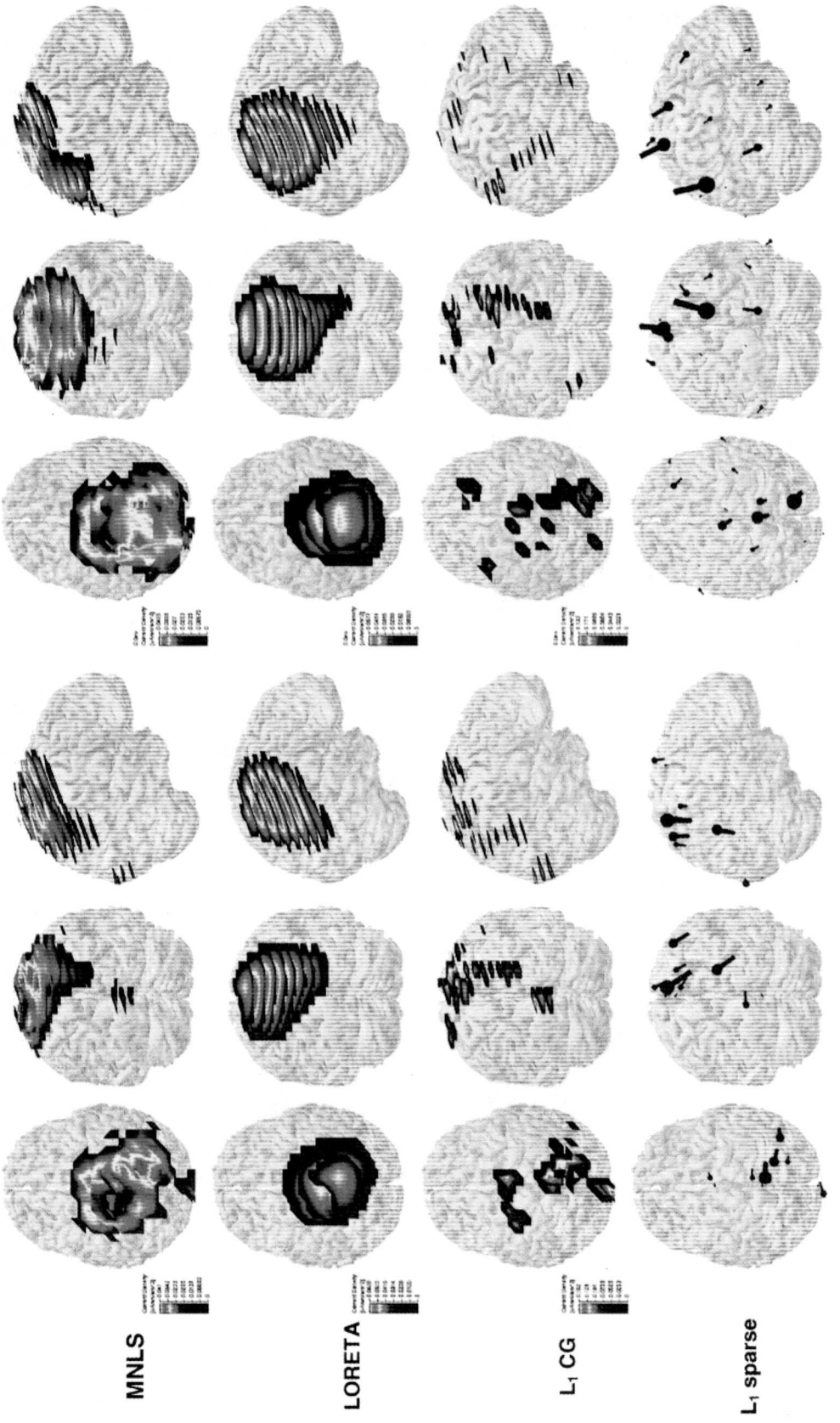

FIG. 20. Linear and nonlinear current density reconstructions on three-dimensional grids (7 mm, 5340 nodes) as Fig. 16 for EEG-2. Results are displayed together with the cortical gray matter layer in top, rear, and right views as color coded overlays or poles (L_1 sparse). Top to bottom rows: minimum norm least squares (MNLS), Laplacian smoothness reconstructions (LORETA), L_1 conjugate gradient (CG) (all clipped > 60%), L_1 sparse (20 nAm/mm). Left: −40, right: 0 milliseconds (ms).

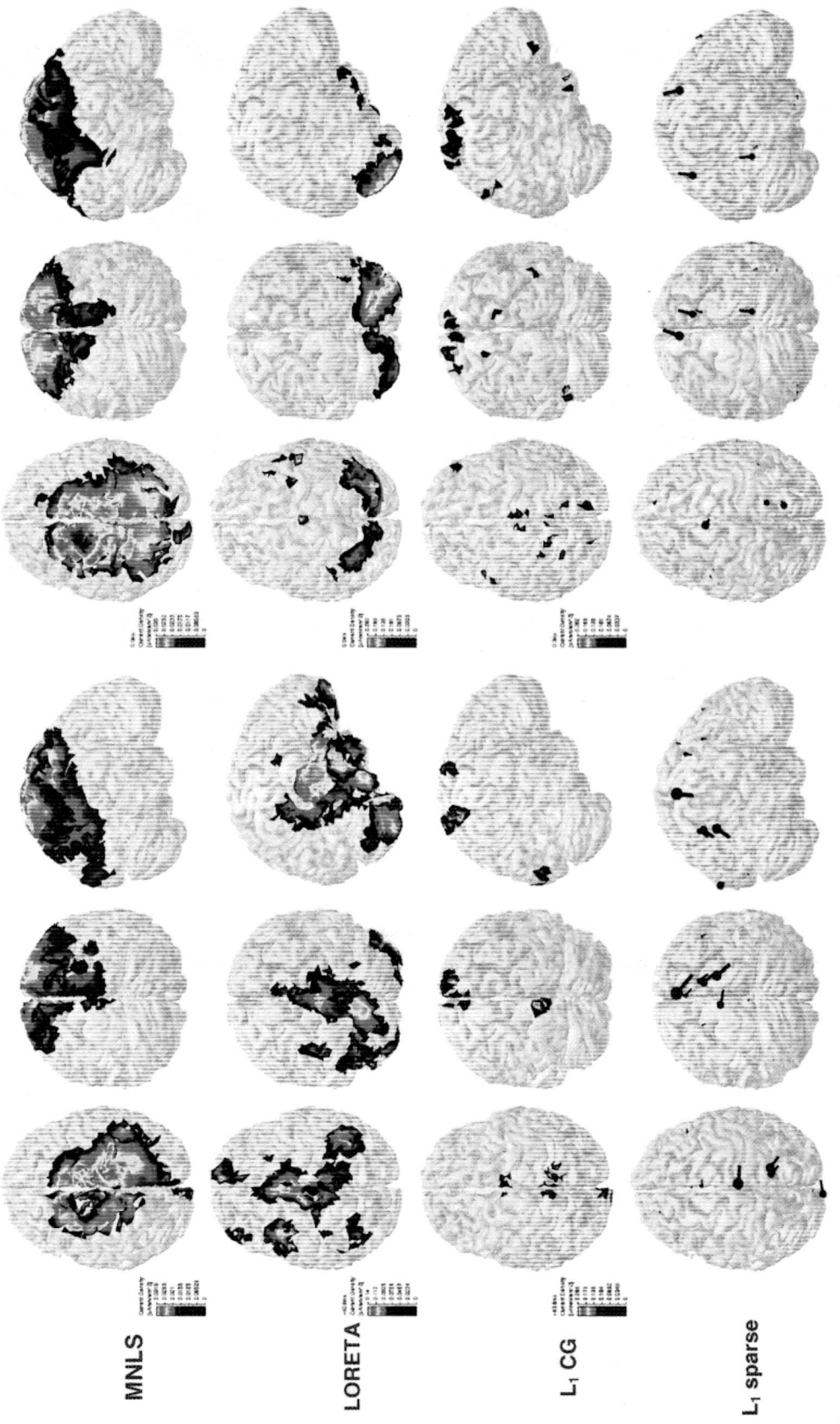

FIG. 21. As Fig. 20, EEG-2, cortically constrained methods, without normals (5.2 mm mean distance, 11,202 nodes). Top to bottom rows: minimum norm least squares (MNLS), Laplacian smoothness reconstructions (LORETA), L_1 conjugate gradient (CG) (all clipped $> 60\%$), L_1 sparse (20 nAm/mm). Left: -40, right: 0 milliseconds (ms).

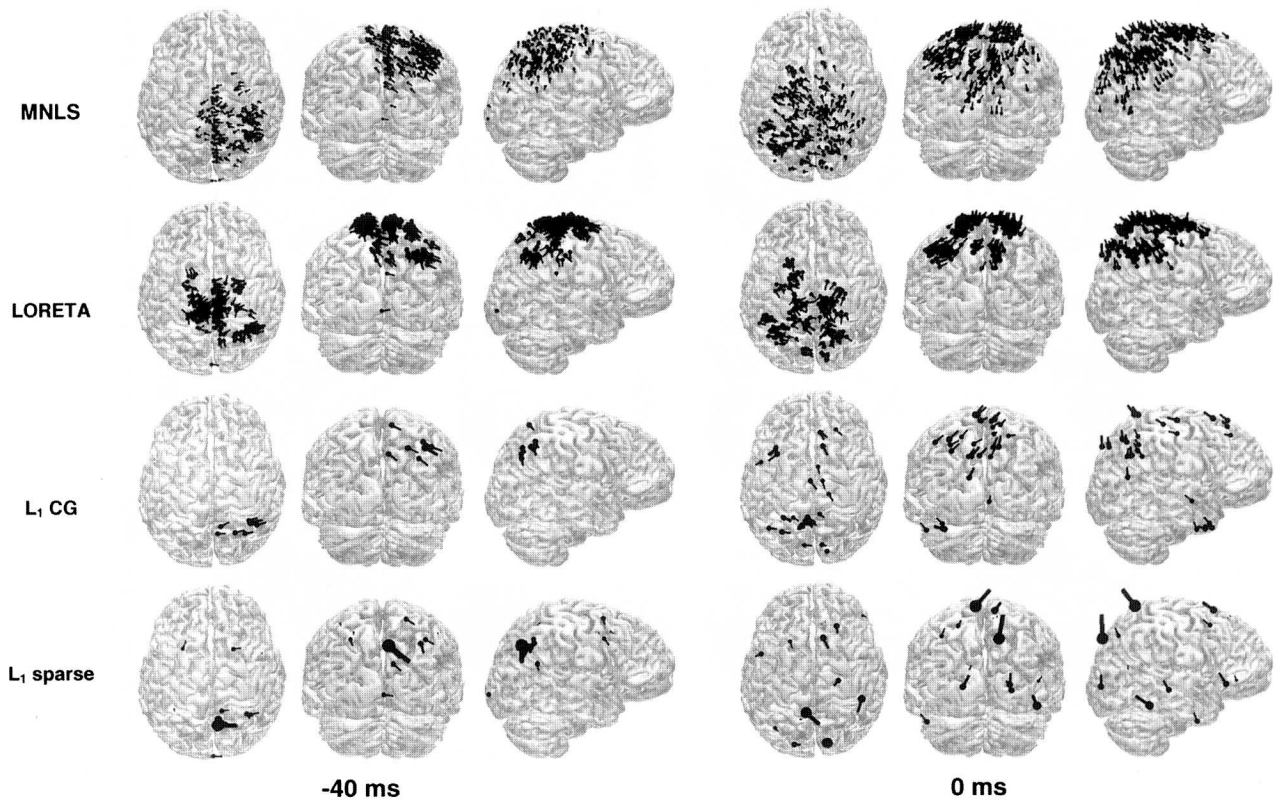

FIG. 22. As. Fig. 21, EEG-2, cortically constrained linear and nonlinear algorithms, with normals. Top to bottom rows: minimum norm least squares (MNLS), Laplacian smoothness reconstructions (LORETA) (clipped > 70%, 1 nAm/mm), L_1 conjugate gradient (CG) (clipped > 70%, 1 to 5 nAm/mm), L_1 sparse (50 nAm/mm). Left: −40, right: 0 millisecond (ms).

resolution for the simulated data. Furthermore, due to the more indirect effect of the source strengths in the model term, lead-field normalization is less critical as compared to the standard MNLS algorithm.

Compared to the linear methods, the nonlinear approaches exhibit better localization accuracy and improved spatial resolution at high SNRs. The interpretation of the results is more difficult, since especially at small SNRs and with the L_1-sparse approach a few, relatively strong dipoles are reconstructed close to or around the true source location and no smooth distributions with approximately matching center positions can be seen.

For the more realistic low SNR cases spatial resolution and localization accuracy decrease for all methods studied and at deep source positions the reconstructed current

TABLE 1. *Computational efforts for the different BEM models, lead-field matrix set-up, and reconstruction algorithms*

BEM-model No. of nodes/triangles	BEM setup [s]	BEM-matrix decompose [s]	IPA-matrix decompose [s]	Lead-field matrix size (cortical surface)	Lead-field matrix setup [s]	MNLS [s]	LORETA [s]	L_1 CG [s]	L_1 sparse [s]	MUSIC fit (3 dip.) [s]	MUSIC scan (3 dip.) [s]
EEG-1				(9956 nodes)							(24,977 nodes)
4448/8884	300	600	24	29,868 * 27	180	1.3	20	216	50	8.7	6.4
EEG-2				(11,202 nodes)							(25,660 nodes)
3907/7810	230	435	19	33,606 * 26	170	1.5	24	270	45	4.7	6.4

All times are given in seconds for an Intel Pentium II 400MHz PC with 256MB RAM. BEM model and lead-field matrix set-up have to be performed only once. BEM, boundary element method; IPA, isolated problem approach; LORETA, Laplacian smoothness method; MNLS, minimum norm least squares; MUSIC, (multiple signal classification) a spatiotemporal dipole model.

densities develop irregular shapes. The nonlinear L_1-norm algorithm suffers most from low SNRs by showing scattered and spurious results for deep source locations.

Adjusting the regularization parameter, that weights between data and model term, can be performed automatically for the MNLS and L_1-sparse approaches, if the noise of the data is known and specified correctly. All methods are found to be very sensitive to overfitting the data in the realistic SNR cases, since then the algorithms will start to fit the noise or correlated background features of the data. Thus fixed or wrong choices of the regularization parameter will lead to spurious results or ghost sources, that explain more of the data than their signal contents. Small deviations between measured and calculated fields can always be achieved by adjusting small values of the regularization parameter. For current density methods, they are thus no longer a good criterion for the quality of the reconstruction result. It is essential to have a good estimate for the noise in the data and adjust the regularization parameter accordingly.

Unknown Epileptic Spike Data

Finally, all current density reconstruction methods are applied to two unknown epileptic spike data sets. In both cases realistic volume conductor models, segmented from individual anatomic magnetic resonance images, are used. The measured, unaveraged data exhibit a low number of electrodes (27 respectively 26), but nevertheless a good coverage of the upper hemisphere, thus revealing relatively large interelectrode distances. All reconstruction methods are applied with support points on regular 3D grids limited by the innermost compartment of the BEM volume conductor model. The cortical gray matter layers are segmented from the anatomic data to enable cortically constrained reconstructions. To implement even more a priori knowledge the surface normals of these layers can also be used in addition.

The reconstructions from the first data set reveal source activity in left temporal lobe of the patient. As found earlier (Yvert et al., 1997; Fuchs et al., 1998*a*), realistic volume conductor models are essential for temporal lobe source analyses, since otherwise localization errors in the order of 2 to 3 cm, mainly in the vertical direction, result. The early components of the spike seem to originate from the frontal basal region of the left temporal lobe, as all applied methods suggest with more or less spatially resolved details. In conclusion, the results for the first epileptic spike data set all confirm each other and give a similar picture as the spatiotemporal source reconstructions, which should always be performed for comparison. The correct choice of the regularization parameter is critical, especially in low SNR cases or when systematic errors like correlated background activity are present. The properties of the distributed source reconstruction algorithms in this case behave as expected from the idealized simulations. The overfocussing L_1 sparse results should not be overinterpreted, since the remaining few centers of strong activity may be grouped around a real dipolar source or represent the center of unresolvable activated areas only. Including more physiologic a priori knowledge like the cortical gray matter layer normals as orientational constraints improves the results by suppressing sidelobes and cortical patches with wrong orientation. The resolution of all methods is not sufficient to reveal more spatial or temporal details of the epileptic spike development, but this should be seen in the light of the rather limited number of electrodes. Better results as published earlier under even more idealized conditions (Wang et al., 1992) as in our simulations thus cannot be expected here.

The second epileptic spike data set with nearly all source reconstruction methods shows activity at the middle of the upper hemisphere around the interhemispheric gap and the vertex (C_z-electrode, compare Fig. 19). The spatiotemporal and most distributed source reconstructions seem to have their centers slightly shifted to the right hemisphere, but the poor spatial resolution, which is mainly due to the low SNR (where "noise" need not be limited to statistical processes only) and the large interelectrode distances, allow no unique decision. However, looking at the potential maps on the skin (Fig. 4), the results seem to be reasonable.

Care should be taken not to overinterpret the results of the nonlinear algorithms because they may not reflect the true source configurations especially in low SNR cases. This may also be due to the conjugate gradient algorithm used for acceptable performance of some of the methods: the choice of convergence criteria may be critical. The best approach is to compare all methods available to come to a more settled conclusion and not to rely on a single method that worked well in a special case. One should also keep in mind, that the inverse problem has no unique solution, but that physiologically meaningful source models are needed the achieve an appropriate result.

An adequate choice of the regularization parameter is very important and has to rely on trustable estimates of the SNR and/or the background signals. Finally, looking at the strongly underdetermined character of the problems (about thousand times more unknowns than measured data), a limited spatial resolution is expectable, since the number of source distributions, that form the result by linear combination, is less or equal to the

number of sensors used (Jeffs et al., 1988; Köhler, 1998). Thus, high spatial frequencies in the source space domain are rather strongly damped.

All independent source models available should be applied and compared to achieve confirmed results. The limited spatial resolution of current density reconstructions can be improved by an increased number of sensors. However, even with low spatial sampling as in the epileptic spike cases analyzed here, the results shown may confirm classical diagnostic approaches and may help to guide further invasive measurements (e.g. EcoG), which are needed for verification.

Acknowledgment: The authors thank Prof. John Ebersole, Yale University, New Haven for encouraging this paper and for kindly supplying the unknown epileptic spike data.

REFERENCES

Backus GE, Gilbert JF. Numerical Applications of a Formalism for Geophysical Inverse Problems. *Geophys J Royal Astronom Soc* 1967;13:247–76.

Collins DL, Neelin P, Peters TM, Evans AC. Automatic 3D intersubject registration of MR volumetric data in standardized Talairach space. *J Comput Assist Tomogr* 1994;18:192–205.

Dale AM, Sereno MI. Improved localization of cortical activity by combining EEG and MEG with MRI cortical surface reconstruction: a linear approach. *J Cogn Neurosci* 1993;5:162–76.

Dallas W. Fourier Space Solution to the Magnetostatic Imaging Problem. *Appl Opt* 1985;24:4543–56.

de Munck JC, Peters MJ. A fast method to compute the potential in the multisphere model. *IEEE Trans Biomed Eng* 1993;40:1166–74.

de Munck JC, van Dijk BW, Spekreijse H. Mathematical dipoles are adequate to describe realistic generators of human brain activity. *IEEE Trans Biomed Eng* 1988;35:960–6.

Fuchs M, Wagner M, Wischmann HA, Ottenberg K, Dössel O. Possibilities of functional brain imaging using a combination of MEG and MRT. In: Pantev C, ed. *Oscillatory event related brain dynamic*. New York: Plenum Press, 1994*a*:435–57.

Fuchs M, Wischmann HA, Wagner M. Generalized Minimum Norm Least Squares Reconstruction Algorithms. In: Skrandies W, ed. *ISBET Newsletter 5*. Giessen, Germany, 1994*b*:8–11.

Fuchs M, Wagner M, Wischmann HA, Dössel O. Cortical Current Imaging by morphologically constrained Reconstructions. In: Baumgartner C, et al., eds. *Biomagnetism: fundamental research and clinical applications*. Amsterdam: Elsevier Science IOS Press. 1995;320–5.

Fuchs M, Drenckhahn R, Wischmann HA, Wagner M. An Improved Boundary Element Model for Realistic Volume Conductor Modeling. *IEEE Trans Biomed Eng* 1998*a*;45:980–97.

Fuchs M, Wagner M, Wischmann HA, Köhler T, Theiβen A, Drenckhahn R, Buchner H. Improving Source Reconstructions by Combining Bioelectric and Biomagnetic Data. *Electroenceph Clin Neurophysiol* 1998*b*;107:93–111.

Fuchs M, Wischmann HA, Wagner M, Theiβen A. Performance of realistically shaped boundary element method volume conductor models. *Proc BIOMAG '98*. Sendai, Japan, 1998*c*.

Gorodnitzky I, George JS, Schlitt HA, Lewis PS. A Weighted Iterative Algorithm for Neuromagnetic Imaging. *Proc IEEE Satellite Symp Neurosci Technology*. Lyon, France, 1992:60–4.

Grave de Peralta Menendez R, Hauk O, Andino SG, Vogt H, Michel C. Linear inverse solutions with optimal resolution kernels applied to electromagnetic tomography. *Hum Brain Mapping* 1997;5:454–67.

Grave de Peralta Menendez R, Gonzalez-Andino SL. A Critical Analysis of Linear Inverse Solutions to the Neuroelectromagnetic Inverse Problem. *IEEE Trans Biomed Eng* 1998;45:440–8.

Hämäläinen MS, Sarvas J. Realistic conductivity geometry model of the human head for interpretation of neuromagnetic data. *IEEE Trans Biomed Eng* 1989;36;165–71.

Hämäläinen MS, Ilmoniemi RJ. Interpreting magnetic fields of the brain: minimum norm estimates. *Med Biol Eng Comput* 1994;32: 35–42.

Hanke M, Hansen PC. Regularization methods for large-scale problems. *Surv Math Ind* 1993;3:253–315.

Hansen PC. Analysis of discrete III-posed problems by means of the L-curve. *SIAM Review* 1992;34:561–80.

Huiskamp G. Difference formulas for the surface laplacian on a triangulated surface. *J Comp Phys* 1991;95:477–96.

Jeffs B, Leahy R, Singh M. An evaluation of methods for neuromagnetic image reconstruction, *IEEE Trans Biomed Eng* 1987;34: 713–23.

Köhler T. Lösungen des bioelektromagnetischen inversen problems [doctoral thesis]. Technical University, Hamburg, Germany; 1998.

Kullmann W, Dallas W. Fourier imaging of electrical currents in the human brain from their magnetic fields. *IEEE Trans Biomed Eng* 1987;34:837–42.

Lawson CL, Hanson RJ. *Solving least squares problems*. New Jersey: Prentice Hall, 1974.

Luenberger DG, Kuenberger DG. *Linear and nonlinear programming*, 2nd ed. Addison-Wesley, 1984.

Matsuura K, Okabe Y. Selective minimum-norm solution of the biomagnetic inverse problem. *IEEE Trans Biomed Eng* 1995;42: 608–15.

Matsuura K, Okabe Y. L_p-normalized Minimum L_1-norm solution of the biomagnetic inverse problem. *Proc IEEE Eng Med Biol Soc*, Nijmegen, The Netherlands, 1996.

Matsuura K, Okabe Y. A robust reconstruction of sparse biomagnetic sources. *IEEE Trans Biomed Eng* 1997;44:720–6.

Messinger-Rapport BJ, Rudy Y. Regularization of the inverse problem in electrocardiography: a model study. *Math Biosci* 1988;89:79–118.

Morozov VA. The error principle in the solution of operator equations by the regularization method. *USSR Comp Math Math Phys* 1968;28:69–80.

Mosher JC, Lewis PS, Leahy RM. Multiple dipole modeling and localization from spatio-temporal MEG data. *IEEE Trans Biomed Eng* 1992;39:541–57.

Mosher JC, Leahy RM. Recursive MUSIC: A framework for EEG and MEG source localization. *IEEE Trans Biomed Eng* 1998;45: 1342–54.

Nelder JA, Mead R. A simplex method for function minimization. *Comput J* 1965;7:308–13.

Pascual-Marqui RD, Michel CM, Lehmann D. Low resolution electromagnetic tomography: a new method for localizing electrical activity in the brain. *Int J Psychophysiol* 1995;18:49–65.

Pflieger ME, Simpson GV, Ahlfors SP, Ilmoniemi RJ. Superadditive information from simultaneous MEG/EEG data. In: Aine C, Okada Y, Stroink G, Swithenby S, Wood C, eds. *Advances in Biomagnetism Research: Biomag96*. New York: Springer-Verlag, 1999 (in press).

Phillips JW, Leahy RM, Mosher JC. MEG-based imaging of focal neuronal current sources. *IEEE Trans Med Imaging* 1997;16:338–48.

Scales JA, Gersztenkorn A, Treitel S. Fast Ip solution of large, sparse linear systems: application to seismic travel time tomography. *J Comp Phys* 1988;75:314–33.

Scherg M, von Cramon D. Two bilateral sources of the late AEP as identified by a spatio-temporal dipole model. *Electroenceph Clin Neurophysiol* 1985,65:32–44.

Scherg M, Ebersole JS. Models of brain sources. *Brain Topogr* 1993; 5:419–23.

Sekihara K, Scholz B. Generalized wiener estimation of three-dimensional current distribution from biomagnetic measurements. *IEEE Trans Biomed Eng* 1996;43:281–91.

Smith WE, Dallas WJ, Kullmann WH, Schlitt HA. Linear estimation theory applied to the reconstruction of a 3-D vector current distribution. *Appl Opt* 1990;29:658–67.

Tarantola A. *Inverse problem theory*, 2nd ed. Amsterdam: Elsevier, 1994.

Wagner M, Fuchs M, Wischmann HA, Ottenberg K, Dössel O. Cortex segmentation from 3D MR images for MEG reconstructions. In: Baumgartner C, et al., eds. *Biomagnetism: fundamental research and clinical applications.* Amsterdam: Elsevier Science IOS Press, 1995:433–8.

Wagner M, Fuchs M, Wischmann HA, Drenckhahn R, Köhler T. Smooth reconstrcutions of cortical sources from EEG and MEG recordings. *NeuroImage* 1996;3:168.

Wagner M. Rekonstruktion neuronaler Ströme aus bioelektrischen und biomagnetischen Messungen auf der aus MR-Bildern segmentierten Hirnrinde [doctoral thesis]. Aachen, Germany: Shaker Verlag, 1998.

Wang JZ, Williamson SJ, Kaufmann L. Magnetic source images determined by a lead-field analysis: the unique minimum-norm least-squares estimation. *IEEE Trans Biomed Eng* 1992;39: 665–75.

Yvert B, Bertrand O, Thevenet M, Echallier JF, Pernier J. A systematic evaluation of the spherical model accuracy in EEG dipole localization. *Electroenceph Clin Neurophysiol* 1997; 102:452–9.